Slug Flow Characterization in an Alkaline Water Electrolyzer for Hydrogen Production

ME55035: ME-EFPT MSc Thesis

Mehmet Caner Pektas

Delft University of Technology

Slug Flow Characterization in an Alkaline Water Electrolyzer for Hydrogen Production

by

Mehmet Caner Pektas

to obtain the degree of Master of Science
at the Delft University of Technology,
to be defended publicly on Friday April 21, 2023 at 09:30 AM.

Student number:	4441540	
Project duration:	May, 2022 – April, 2023	
Thesis committee:	Dr. ir. J. W. Haverkort,	TU Delft, supervisor
	Dr. L. Botto,	TU Delft
	Dr. A. Laskari,	TU Delft

This thesis is confidential and cannot be made public until April 20, 2025.

Preface

I am delighted to present this report, which is the culmination of months of hard work and dedication. I would like to take this opportunity to express my sincere gratitude to everyone who has supported and encouraged me throughout this endeavor.

Firstly, I would like to express my sincere appreciation to both of my supervisors. Firstly, to my academic supervisor, Dr.ir. J.W. Haverkort, thank you for your invaluable guidance, patience, and support throughout this project. Your expertise and insight have been critical in shaping my approach and understanding. Additionally, I would like to thank my supervisor from ERIKS, T. Blik, who provided me with help and encouragement in the preparation and construction of my final product.

I also would like to thank all participants who generously gave their time and contributed to this study. Their willingness to share their experiences and insights has been invaluable and I am deeply grateful for their contributions. Without the support and assistance of these wonderful people, this report would not have been possible.

I am thankful for the companionship of my friends who made my academic journey even more pleasurable. Lastly, I owe a debt to my family for their unwavering love and support and to my girlfriend for her understanding and patience during times of stress and pressure. Your constant encouragement and belief in me have been a source of strength and motivation.

Mehmet Caner Pektas
Delft, April 2023

Abstract

A water electrolyzer is an electrochemical device that produces hydrogen and oxygen from water via electricity. A sustainable way of producing hydrogen with renewable electricity, also known as green hydrogen, could enable its use in decarbonisation of sectors that depend on fossil fuels. However, to scale up the production of green hydrogen, larger water electrolyzers are required, which presents challenges. Water electrolyzers produce hydrogen in the form of bubbles, which are transported away through outlet channels. The geometry of the outlet channel is important for performance and safety. A channel that is too wide can result in unwanted ionic current leakage, reducing efficiency and increasing the risk of explosion. To reduce the leakage current, the electrical resistance in the channel can be increased to make it difficult for ions to flow through. However, a narrow channel can increase the hydraulic resistance, leading to clogging due to bubble build-up.

This study focuses on the characterization of the slug flow regimes that eventually lead to clogging of the outlet channel in a novel electrolyzer design. To characterize the flow when blockage develops, electrochemical tests with industrially relevant 6M KOH were carried out at room temperature and ambient pressure in conjunction with high-speed video recording. The examined channel was 2 mm high, 3 mm wide, and 40 mm long. The experiments showed that clogging occurs for certain flow regimes. The hydraulic configuration caused clogging at the hydrogen side, which caused the liquid flow prefer to travel via the anode rather than the cathode, which was reflected in the temperature plots. Clogging did not occur when the superficial gas velocity was greater than 0.3 cm/s, which corresponds to a current density of 140 mA/cm^2. The clogging was also not visible at a superficial liquid velocity greater than 0.25 cm/s. Below these values, clogging is expected to take place for the investigated channel dimensions. The bubble diameters in the bubble layer in front of the channel were measured with a microscopic camera. The mean bubble diameter was 0.4 mm, which is 80% smaller than the height of the channel through which they flow. However, exceptional bubble sizes that were 3 to 4 times the channel height, which ultimately led to clogging of the channel, were also present. The bubble layer thickness and velocity at increasing liquid flow rates and current densities were measured using a high-speed camera. At low current densities, the velocity and thickness of the bubble layer were not affected by the liquid flow rate. At higher current densities, a higher liquid flow rate appeared to reduce the thickness of the bubble layer, but not the velocity of the bubble layer. The bubble layer thickness as well as the velocity strongly depend on the applied current density (and thus the gas flow velocity).

This knowledge might be, when the flow regimes are scaled to larger electrolyzer dimensions accordingly, essential for future electrolyzer manufacturers and operators for the operation and design of larger-scale electrolyzers. It will give insight into which flow regimes should be avoided in order to avoid clogging and thus explosion risks during operation.

Contents

List of Figures

List of Tables

Nomenclature

Abbreviations

Abbreviation	Definition
AWE	Alkaline Water Electrolyzer
PEMWE	Proton Exchange Membrane Water Electrolyzer
SOEL	Solid Oxide Water Electrolyzer
HER	Hydrogen Evolution Reaction
OER	Oxygen Evolution Reaction
HSV	High Speed Video

Greek symbols

Symbol	Definition	Unit
α	Charge transfer coefficient	[-]
β	Ratio of resistance via cell to resistance via bypass conductor	[-]
η	Overpotential	[V]
ϵ	Porosity	[-]
κ	Conductivity	[S m^{-1}]
ψ	Ratio of bypass current to total cell current	[-]
θ	Minimum current ratios for a cell assembly	[-]
τ	Tortuosity	[-]

Symbols

Symbol	Definition	Unit
a	Activity	[-]
A	Surface area	[m^2]
c	Concentration	[mol L^{-1}]
i/I	Current	[A]
j	Current density	[A m^{-2}]
j_0	Exchange current density	[A m^{-2}]
l	Interelectrode gap	[m]
n	Number of electrons exchanged	[-]
N	Number of cells in an electrolyzer stack	[-]
p	Pressure	[Pa]
T	Temperature	[K]
U_{cell}	Applied cell potential	[V]
U_{eq}	Equilibrium potential	[V]
H_0	Standard enthalpy of formation	[J mol $^{-1}$]
G_0	Gibbs free energy	[J mol $^{-1}$]
S_0	Standard entropy	[J K^{-1} mol $^{-1}$]

Constants

Symbol	Definition	Magnitude	Unit
p_0	Standard pressure	1	[Pa]
F	Faradays constant	96485	[C mol^{-1}]
R	Gas constant	8.314	[J K^{-1} mol^{-1}]

1

Introduction

Global fossil CO_2 emissions increased further in 2022, returning to pre-COVID 2019 levels after a dip caused by the COVID-19 pandemic. Figure 1.1 depicts a chart showing the upward trend in global fossil carbon emissions over the past 60 years [1].

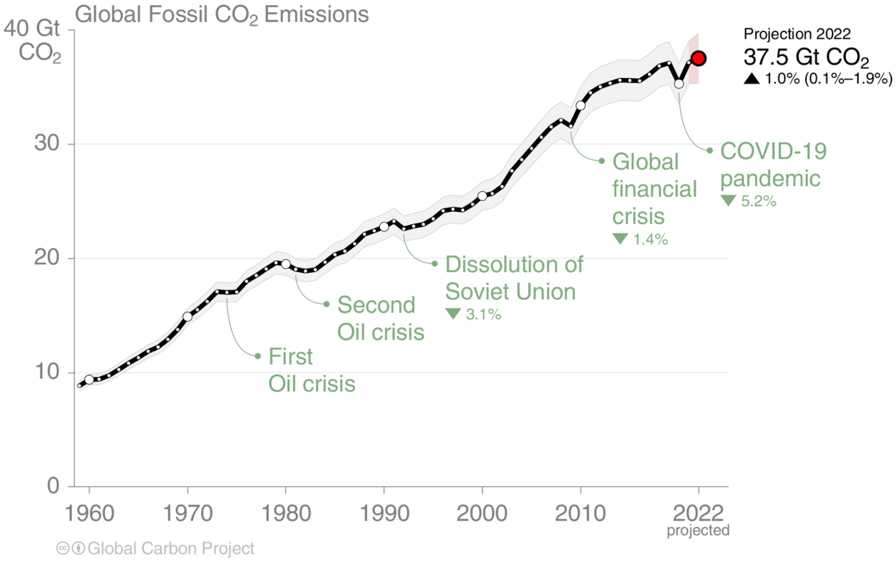

Figure 1.1: Global fossil CO_2 emissions over the past 60 years [1].

Due to the universal goal of adhering to the Paris Agreement [2], which aims to globally limit CO_2 emissions from fossil fuels, alternative sustainable energy sources such as hydrogen have gained in popularity. Hydrogen can, for example, provide an alternative for sectors where fossil fuels are still utilized, such as transportation, householding, and industry. Hydrogen vehicles, for example, already exist and are legal on the road. Other examples of hydrogen applications are recent pilot projects in several Dutch neighborhoods where natural gas is replaced by hydrogen fuel [3]. Similarly, for industrial production processes that still require steam or hot water, hydrogen-fed boilers may provide the option of burning hydrogen instead of natural gas [4]. Moreover, when hydrogen is produced by performing water electrolysis, it is also possible to generate hydrogen when there is an excess of electricity on the grid and store the hydrogen until it can be converted back to electricity, via fuel cells, once there is a shortfall.

These large-scale hydrogen applications require large-scale, but more essential, sustainably produced hydrogen from renewable energy sources. This type of hydrogen is also known as "green hydrogen". A sustainable way to produce green hydrogen is, for instance, through water electrolysis, in which electricity is the only energy source needed to decompose water into hydrogen and oxygen gas. The three most common types of water electrolyzers are the PEM water electrolyzer (PEMWE), alkaline water electrolyzer (AWE), and the solid-oxide

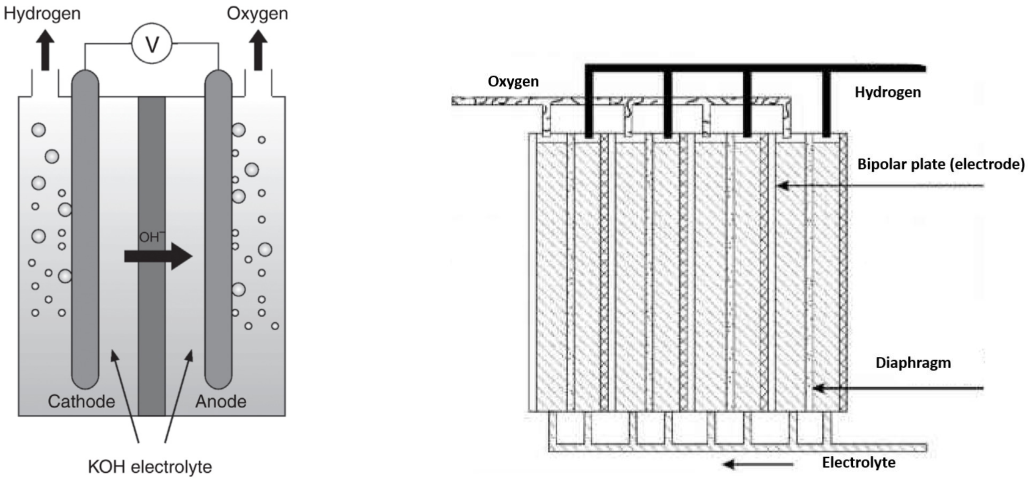

(a) (b)

Figure 1.2: A single electrolysis cell [5] (a) and a stack of multiple tightly packed cells [6] (b)

water electrolyzer (SOWE). Alkaline water electrolysis is the form of electrolysis that is examined in this report because it has the greatest potential to reduce the cost of hydrogen generation compared to the other types.

A schematic of an alkaline water electrolyzer cell is provided in Figure 1.2a. It consists of two electrodes submerged in an electrically conductive water solution (electrolyte), and when a sufficiently high voltage difference is applied to the electrodes, ionic current will run through the electrolyte and the following two half reactions will take place at the two electrodes:

$$\begin{array}{rcll} 4\mathrm{OH}^-(\mathrm{l}) & \rightarrow & \mathrm{O}_2(\mathrm{g}) + 2\mathrm{H}_2\mathrm{O}(\mathrm{l}) + 4\mathrm{e}^- & \text{Anode} \\ 4\mathrm{H}_2\mathrm{O}(\mathrm{l}) + 4\mathrm{e}^- & \rightarrow & 2\mathrm{H}_2(\mathrm{g}) + 4\mathrm{OH}^-(\mathrm{l}) & \text{Cathode} \\ \hline 2\mathrm{H}_2\mathrm{O}(\mathrm{l}) & \rightarrow & 2\mathrm{H}_2(\mathrm{g}) + \mathrm{O}_2(\mathrm{g}) & \text{Total reaction} \end{array} \tag{1.1}$$

Hydrogen and oxygen are produced in the form of gas bubbles. The presence of these generated bubbles reduces the efficiency of electrolysis, and therefore, it is desired to transport the bubbles away as quickly as possible. A diaphragm separates the bubbles produced because a mixture of hydrogen and oxygen increases the risk of explosion. To increase hydrogen production, multiple electrolyzer cells can be tightly packed together in a stack, as shown in Figure 1.2b.

1.1. A novel electrolyzer

Recently, a type of water electrolyzer stack was designed and built by a group of bachelor students at the Process & Energy department of TU Delft [7]. The advantage of this design, which was originally developed and patented by J.W. Haverkort, [8], is the fact that the cells are interconnected in series with one another such that the anodes and cathodes alternate among two cells rather than alternating with each cell, which is often applied in conventional electrolyzers. Less alternation between cells makes the process safer because the compartments carrying the produced gases are less exposed to each other. Furthermore, the electrodes used were corrugated in shape (i.e. waved), as suggested in patent [8], in order to increase the reaction surface area and thus the hydrogen produced per volume taken by the electrolyzer.

1.2. Problem statement

As depicted in Figure 1.2b, exit channels of the cells share common manifolds, which pose prevalent issues and design constraints in electrolyzer stacks. For instance, the ionic current that is used to flow between electrodes in a cell can make use of the shared manifold to flow to other cells as well. This undesirable ionic current is known as a “leakage” or a “shunt” current and reduces the efficiency of an electrolyzer stack. Moreover, the potential difference over the electrodes can be turned in sign, causing an intended anode (connected to an outlet manifold with O_2) to behave as a cathode to produce H_2. A switch in electrode polarity can increase the risk of an explosion. From this perspective, bubbles are advantageous because they increase the electrical resistance in exit channels and therefore reduce the risk of explosion or fire. However, because of excessive bubble accumulation, the exit channel might become clogged, preventing products from leaving. These gas remnants that are left behind might come into contact with the dry, hot electrode surface, creating explosive hazards. Moreover, the dry part of the electrode surface causes the current density to increase locally and as a result, the temperature, posing a fire risk. Therefore, it is crucial to understand the behavior of bubble buildup and leakage currents to maximize both the efficiency and safety of the operation.

In an electrolytic cell, the dimensions of the exit channel affect both the shunt current and the flow rate of bubbles through the channel. A narrow channel gives a larger electrical resistance and consequently reduces the shunt currents at a given potential. On the contrary, narrowing the channel increases hydraulic resistance, which impedes the flow rate at a given pressure drop. Figure 1.3 shows images of how hydrogen bubbles accumulate until they form slugs that ultimately block the channel completely in an electrolytic cell.

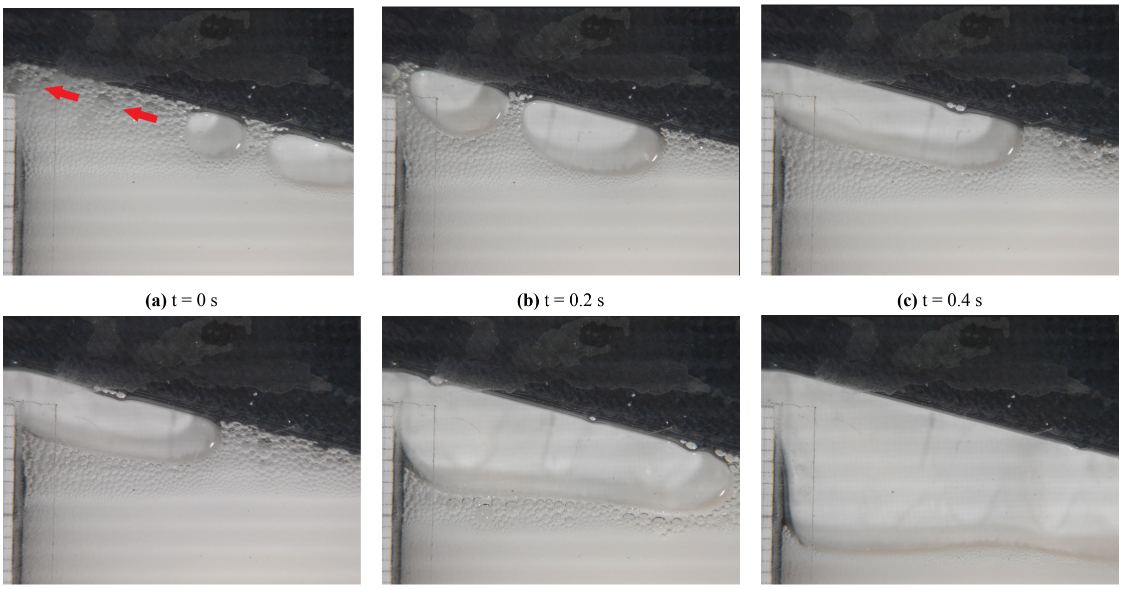
(a) t = 0 s **(b)** t = 0.2 s **(c)** t = 0.4 s

(d) t= 0.5 s **(e)** t= 5 s **(f)** t= 15 s

Figure 1.3: Sequence of images at different time points of hydrogen bubble layer flow when clogging takes place. (a) and (b) demonstrate two large bubbles expanding as they move towards the exit channel. The flow direction is indicated with red arrows in (a). In (c), the two large bubbles coalesce and form a large slug that blocks the entire outlet channel. The slug continues to expand as shown in (e) and (f). All photos include a 1-mm grid on the left side.

The size distribution of bubbles can be a key factor in influencing the overall system performance in many processes involving gas-liquid interactions. For instance, in water electrolysis, the size distribution of gas bubbles might affect the electrode stability and durability, as well as the hydrogen generation efficiency. However, the bubble size distribution is not always uniform throughout the volume of the liquid and can change depending on the geometry of the system, the local gas flow rate, and the liquid properties. Thus, it is necessary to look at the bubble size distribution as a function of height inside the liquid volume. The characteristics of the bubble layer in gas-liquid systems are significantly influenced by both the gas flow rate and the liquid flow rate.

The rate of bubble production and the distribution of bubble sizes are greatly affected by the velocity of gas flow. The bubble layer is often thin and composed of larger, more stable bubbles at low gas flow velocities. Higher gas flow rates may result in smaller, more unstable bubbles and a thicker bubble layer. This happens because bubbles may fragment to smaller sizes as a result of the shear forces produced by the gas flow. Consequently, an increase in gas flow often results in more tiny bubbles, which can improve the efficiency of mass transfer, but also increase the risk of clogging.

The liquid flow rate also plays an important role in determining the behavior of the bubble layer. At low liquid flow rates, the bubble layer may become thicker due to the accumulation of bubbles in the channel. In addition, low liquid flow rates can also promote bubble coalescence, leading to the formation of larger and more stable bubbles. Higher liquid flow rates, on the other hand, can help break up the bubble layer and promote the removal of bubbles from the system.

Therefore, careful control and finding the optimal values of these parameters are important in order to minimize the risk of clogging and other flow instabilities.

1.3. Scope and research questions

This MSc thesis project focuses on the flow characterization of channel blockages in an up-scaled version of the novel electrolyzer design. A larger and improved version of the previous mentioned prototype was designed and built. The design was made so that it was possible to visually inspect the flow within the compartments and outlet channels of the end cells. Furthermore, the electrolyzer was also designed so that the shunt currents could be measured using reference electrodes. The thesis project aims to answer the following main research question:

What are the minimal flow conditions required to keep the clogging in the outlet channel under control?

The following sub-questions need to be answered in order to answer the main question:

1. How are the bubbles distributed and what are their sizes? How are they transported away?
2. What are the effects of the superficial gas and superficial liquid velocity on the gas layer thickness towards the outlet channel?
3. What are the optimal flow conditions to eliminate the thickness of the gas layer?

1.4. Methodology

The thesis began with research in the literature to gain knowledge of water electrolysis and its limitations, such as shunt currents and bubble accumulation. A larger version of the novel electrolyzer was then designed and manufactured. Company ERIKS provided their knowledge and supplies to construct a leak-tight electrolyzer. Experiments were conducted with respect to clogging and slug formation in the outlet channels and were limited to a single cell electrolyzer. The results were then analyzed and conclusions were drawn. Further recommendations were provided for future analysis/improvements.

1.5. Structure of the report

The report consists of 5 chapters. The topic of the thesis project is introduced in Chapter 1. An overview of the fundamentals of water electrolysis, shunt currents, and bubble flow is provided in Chapter 2. In Chapter 3, the procedure for designing and building the electrolyzer is described. This chapter also explains how the experiments were carried out. The experiment results are presented in Chapter 4. The conclusion and recommendations are covered in Chapter 5.

2

Theory

This chapter will discuss the fundamentals of AWE, shunt currents, and vertical bubble transport in water electrolyzers.

2.1. Fundementals of alkaline water electrolysis

2.1.1. Working principle of an alkaline water electrolyzer

In AWE, the hydroxide ions (OH^-) travel from the cathode to the anode via the present diaphragm, as shown in Figure 1.2a. Hydroxide ions are employed as current-carrying species between electrodes. In order to increase the ionic conductivity of the liquid, alkaline compounds are added to the demineralized water. This aqueous solution is often referred to as the electrolyte. In AWE, the added compound is usually potassium hydroxide (KOH) or sodium hydroxide (NaOH) due to its high conductivity. Generally, the electrolyte contains 30 wt% dissolved potassium-hydroxide (KOH). In such a way, higher density of charge-carrying ions is attainable within the electrolyte [9]. While ions travel from cathode to anode in the liquid, the released electrons at the anodic electrode travel via the power supply to the cathodic electrode.

The diaphragm between the electrodes separates gaseous oxygen bubbles and hydrogen bubbles formed while transmitting water molecules and hydroxide and potassium ions (K^+). Separation of the gases produced is essential as a mixture can cause explosion hazards [10]. Therefore, an ideal diaphragm should have a high ionic conductivity, separate the produced gases sufficiently, and be mechanically and chemically stable. These properties depend on the atomic structure, thickness, porosity, and wettability of the diaphragm [11, 12]. Wetting the diaphragm is of importance because, in dried conditions, the produced bubbles tend to stick to the diaphragm-surface and form a blanket made of gas, which increases the ionic resistance. This is also referred to as the ”gas-blanket effect” [13]. The Zirfon PERL separator is an example of a good separation diaphragm that is frequently used in AWE, although its resistance has been shown to be higher when the cells are very tightly packed [14].

Electrode pairs should ideally be made of a material that is electrically conductive, maintains stability under high alkaline conditions, has great catalytic properties, and is easy to acquire. Stainless steel, for example, is inexpensive and easy to access, but does not have great corrosion resistance in alkaline solutions [9]. Nickel, however, is a popular metal that meets the aforementioned demands, and is therefore frequently used in alkaline electrolyzers.

The alkaline water electrolyzer is a well-known and mature type of electrolyzer. Recent developments, such as zero-gap systems and cutting-edge electrode technologies, have further improved the performance of these electrolyzers [15].

2.1.2. Zero-gap configuration

The distance between the electrodes in an electrolyzer is also known as the interelectrode gap. It is the gap in which the hydroxide ions have to travel to reach the anode. The distance between the electrodes results in an electrolytic resistance, which can be computed using the following equation [16] :

$$R = \frac{l}{A\kappa} \tag{2.1}$$

where *l* is the inter-electrode gap, A is the cross-sectional area where the ions flow through, and κ is the electrical conductivity. The equation indicates that the resistance is proportional to the interelectrode gap. Therefore, it is desired to decrease the interelectrode gap as much as possible. In traditional electrolyzers, as shown in Figure 2.1a, the interelectrode gap is relatively large (order of cm) compared to electrolyzers based on the zero-gap principle. A zero-gap design implies that perforated electrodes are pressed against each other with a diaphragm in between, as indicated in Figure 2.1b.

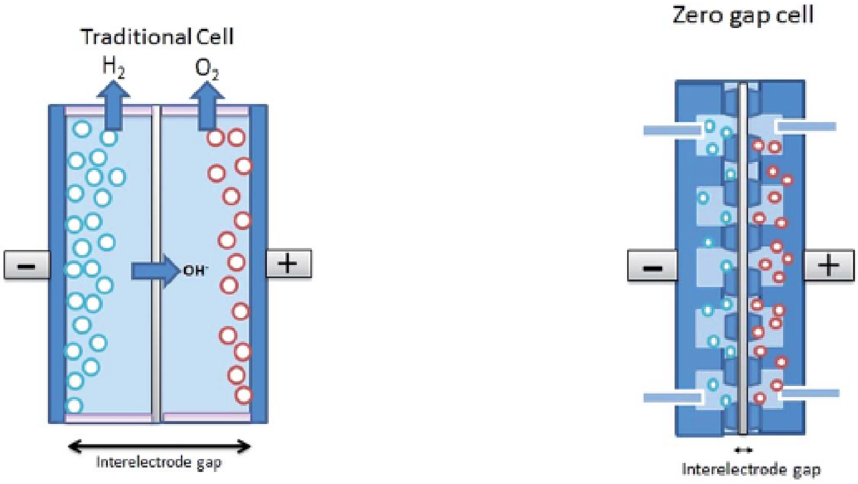

(a)

(b)

Figure 2.1: A traditional cell (a) and a zero-gap cell (b) [16]

.

The zero-gap design for alkaline electrolyzers was first introduced by Zdansky-Lonza in the 1950s [17]. Fundamentally, this means that there is no interelectrode gap (zero-gap) between the electrodes with the exception of the diaphragm thickness. It results in a smaller ohmic resistance between the electrodes, and consequently larger current densities at lower overpotentials (losses) are possible. In addition, a zero-gap design favors a more compact cell and subsequently leaves a smaller footprint compared to traditional designs.

In practice, however, a minor gap between the electrodes is desired to allow bubbles to escape freely and not get trapped between the electrode and diaphragm. Refs. [18] found that for flat plates without holes, there is an optimum distance between electrodes to minimize the overpotential. At large current densities, it was found that a distance of at least 2 mm between the electrodes was necessary to minimize the overpotential and that at smaller gaps, the resistance increased due to larger void (gas) fraction between electrodes. However, at low current densities, it was observed that the overpotential continued to decrease as the gap narrowed. The gas-void fraction was rather low, which explains why the overpotential was not significantly impacted by the smaller gap. In addition, it was observed that the overpotential also increased with the height of the plate. This results from an increase in bubble build-up at uniform mass flux on the upper side of taller electrodes, resulting in a larger gas void fraction [18]. As a result, for taller electrodes, a higher overpotential is required. For perforated electrodes in a zero-gap, Refs. [19] found that a distance of 0.2 mm between the electrodes sufficed to reduce the ohmic losses due to bubbles. Perforations in the electrodes facilitate bubble transport, which ultimately leads to reduced bubble resistance.

2.1.3. Thermodynamics

The reactions in Equation 1.1 can only occur if a sufficiently large potential difference is applied. This results from the fact that the electrochemical reaction of water electrolysis is thermodynamically unfavorable. For a chemical reaction, the required energy can be calculated with the Gibbs equation as shown in Equation 2.2.

$$\Delta H_0 = \Delta G_0 + T_0 \Delta S_0 \tag{2.2}$$

where, ΔH_0 is the change in the standard enthalpy of formation, which is also known as the total required energy. ΔH_0 for water electrolysis is equal to 286.03 $\mathrm{kJ\,mol^{-1}}$. ΔG_0 is the change in standard Gibbs free energy and forms the electric energy demand for the reaction. ΔG_0 is also the minimum required potential for electrolysis, which means that below this potential, hydrogen production is impossible. In addition, this potential represents

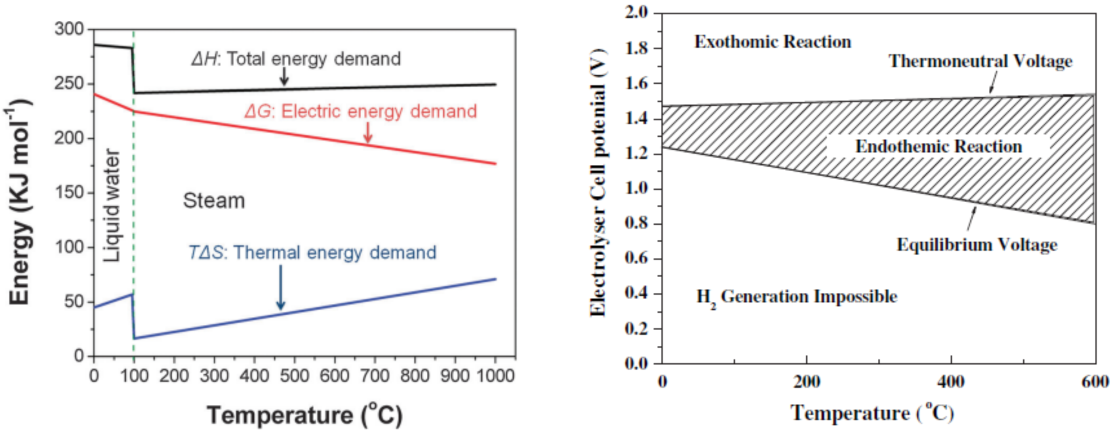

(a) (b)

Figure 2.2: Energy demand (a) and cell potential (b) for electrolysis as a function of temperature [21].

the reversible thermodynamic work, i.e., the useful work that can be recovered when the reverse reaction takes place.

ΔS_0 is the change in entropy. The entropic term represents the thermal part of the equation and represents the phase transition of the liquid reactant (H_2O) to the gaseous products (H_2 and O_2) [20]. The thermal heat input can originate from a heat source or can be provided electrically (ohmic heating). The change in entropy ΔS_0 for water electrolysis at standard conditions is equal to 0.163 kJ K^{-1} mol^{-1}. With the given values, the change in the Gibbs free energy can be calculated with Equation 2.3.

$$\begin{aligned} \Delta G_0 &= \Delta H_0 - T_0 \Delta S_0 \\ &= 286.03 - 298 \times 0.163 = 237.46\,\text{kJ mol}^{-1} \end{aligned} \tag{2.3}$$

Therefore, the electrolysis potential required consists of an electric part (ΔG) and a thermal part ($T\Delta S$). In Figure 2.2a, the relation between ΔH, ΔG and $T\Delta S$ is shown. It appears that as the temperature increases, the thermal energy demand $T\Delta S$ increases. As a consequence, the required demand for electrical energy ΔG is reduced; that is, it is necessary to provide less electrical energy at elevated temperatures, which can also be interpreted as higher electrical efficiency. However, one needs a heat source (e.g. waste/solar/geothermal heat) to achieve such high temperatures.

Once sufficient heat is provided so that the standard enthalpy of formation ΔH_0 is established, the reaction can continue. The corresponding potential (voltage) is defined as the thermoneutral potential, because the reaction does not consume or release thermal energy at this potential. This definition could be misleading because, in reality, the reaction consumes heat up to the thermoneutral potential and thus is endothermic between the minimum and the thermoneutral potential. The thermoneutral potential U_{tn} for water electrolysis can be calculated with Equation 2.4.

$$\begin{aligned} U_{\text{tn}} &= -\frac{\Delta H_0}{nF} \\ &= -\frac{286.03\,\text{kJ mol}^{-1}}{2 \times 96485\,\text{C mol}^{-1}} = -1.48\,\text{V} \end{aligned} \tag{2.4}$$

When a greater potential than the thermoneutral potential is provided, the excess potential will not be consumed, but will be released as heat and, therefore, the reaction becomes exothermic. Similarly, the same equation can be used to calculate the potential that is related to the Gibbs free energy (ΔG). At standard conditions, $\Delta G =$ -1.23 V. The voltage required for hydrogen production as a function of temperature is shown in Figure 2.2b. This figure shows that between the equilibrium voltage (ΔG) and the thermoneutral voltage, the reaction is endothermic, while above the thermoneutral voltage it becomes exothermic.

2.1.4. Overpotentials

In subsection 2.1.2, the term overpotential was introduced for the first time. An overpotential represents the driving force of a chemical reaction [10]. The minimum theoretical cell potential at standard conditions is -1.23V. However, due to inefficiencies and kinetics, the cell potential is slightly larger in practice. The overpotential is the term for this additional necessary potential. The total overpotential consists of 3 contributions, which are shown in Figure 2.3.

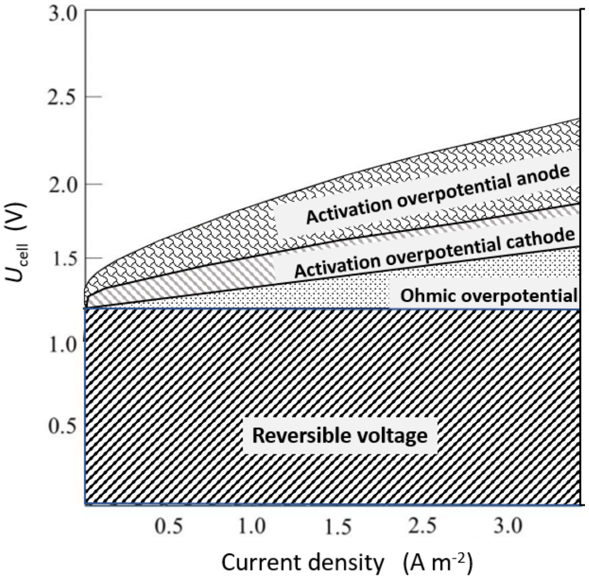

Figure 2.3: The total overpotential consist of 3 terms; the cathodic and anodic activation overpotential, and the ohmic overpotential.

The total overpotential η_{tot} can be expressed as:

$$\eta_{\text{tot}} = U_{\text{cell}} - U_{\text{eq}} = \eta_{\text{act,a}} + \eta_{\text{act,c}} + \eta_{\text{ohmic}} \tag{2.5}$$

where U_{cell} and U_{eq} are, respectively, the cell potential and the equilibrium potential. $\eta_{\text{act,a}}$ and $\eta_{\text{act,c}}$ are the activation overpotentials at the anode and cathode, respectively, and η_{ohmic} is the overpotential due to ohmic resistances. The sum of the activation terms can be calculated with the Tafel equation, given in Equation 2.6, which relates the reaction rate of the electrochemical kinetics to the potential.

$$\eta_{\text{act}} = b\log(\frac{j}{j_0}) \tag{2.6}$$

where j_0 is the exchange current density and b the Tafel slope. These parameters can be obtained experimentally by evaluating the voltage-current characteristics. Further information on the activation overpotential mechanisms and how Tafel parameters are obtained is covered in Appendix A.

The ohmic overpotential η_{ohmic} is caused by ohmic resistance. The ohmic resistance can be classified into electrode, diaphragm, electrolyte, and bubble resistances. With the resistances known, the ohmic overpotential can be determined using Ohm's law:

$$V = \frac{R}{j} \tag{2.7}$$

With all the overpotential terms known, Equation 2.5 can be expressed as:

$$\eta_{\text{tot}} = b\log(\frac{j}{j_0}) + jR \tag{2.8}$$

2.1.5. Cell configuration

Industrial electrolyzers can have dozens of cells that are densely packed together by large, long bolts. The electrodes inside the cells are electrically interconnected. In general, water electrolyzers are classified into two types of electrical configurations, namely the monopolar and bipolar configuration [10]. Schematic illustrations of both arrangements are shown in Figure 2.4.

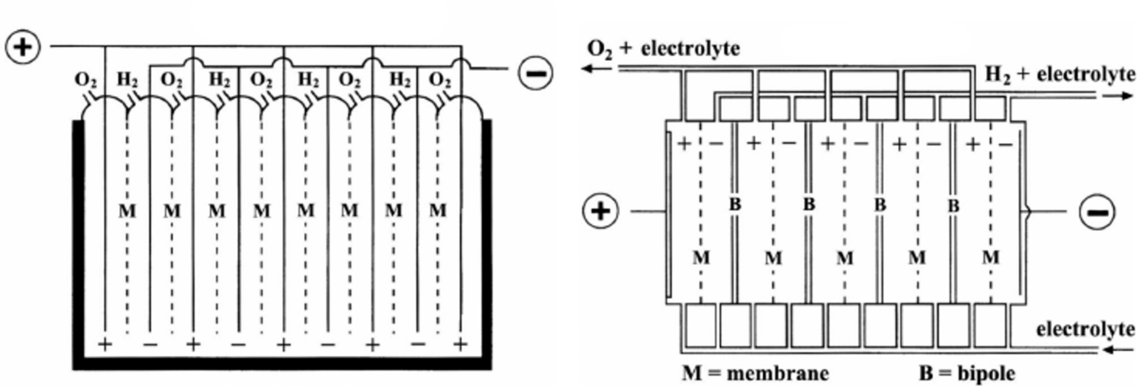

(a)

(b)

Figure 2.4: Monopolar (a) and bipolar (b) configuration of a water electrolyzer stack [21]

A monopolar (unipolar) configuration implies that electrodes have a single (mono) polarity on both sides of the electrode surface. For example, a cathodic electrode will produce hydrogen on both sides of the electrode. As shown in Figure 2.4a, anodes have a parallel connection to the positive terminal of the power supply while the cathodes are connected in parallel to the negative terminal of the power supply. In addition, the total voltage is equal to the voltage in each individual cell, while the total current is equal to the sum of the current in each individual cell. A stack consisting of multiple cells for larger power inputs (order of hundreds of MW) results in higher current flow (thousands of amperes) and therefore higher current (ohmic) losses compared to a stack connected in series [21].

In contrast to the monopolar setup, a bipolar configuration consists of electrodes with opposite (bi-) polarities on each side of the electrode. As shown in Figure 2.4b, the electrodes are connected in series with each other, which means that the total current in the stack is equal to the current through each individual cell. The bipolar stack can operate at higher voltages but at substantially lower currents than the monopolar stack, resulting in significantly lower ohmic losses [22]. Moreover, less voltage conversion, and thus fewer transformers, will be required from an operational point of view.

2.2. Shunt currents

A common issue in electrolyzer stacks is the so-called shunt current, sometimes also referred to as leakage currents, bypass currents, or parasitic currents in the literature. A shunt current is defined as an ionic current that flows from one cell to another not through the diaphragm, but through the feed or exhaust manifold, bypassing neighboring cells where it is supposed to flow [23]. This shunt current is caused by the conductive electrolyte that also flows through the manifolds. Figure 2.5 depicts a schematic illustration of how a shunt current flows in a stack. When the hydraulic resistance through the diaphragm becomes greater than that through the manifold channels, the hydroxide ions will prefer to flow through the latter. As there is less or no electrolysis that will take place in the bypassed cells, a part of the stack will become less active, reducing the total stack efficiency. Furthermore, shunt currents might cause the cathode and anode to be switched, which can lead to electrode corrosion and hence damage the stack. Switching the anode with the cathode and vice versa can also result in a situation where the gases are produced in the same cell, leading to possible explosion hazards [23]. Therefore, to achieve maximum stack performance and safety, the stack should be designed in a way that the shunt currents are minimized or, preferably, prevented. Models that could predict these shunt currents could provide critical insights for electrochemical cell design.

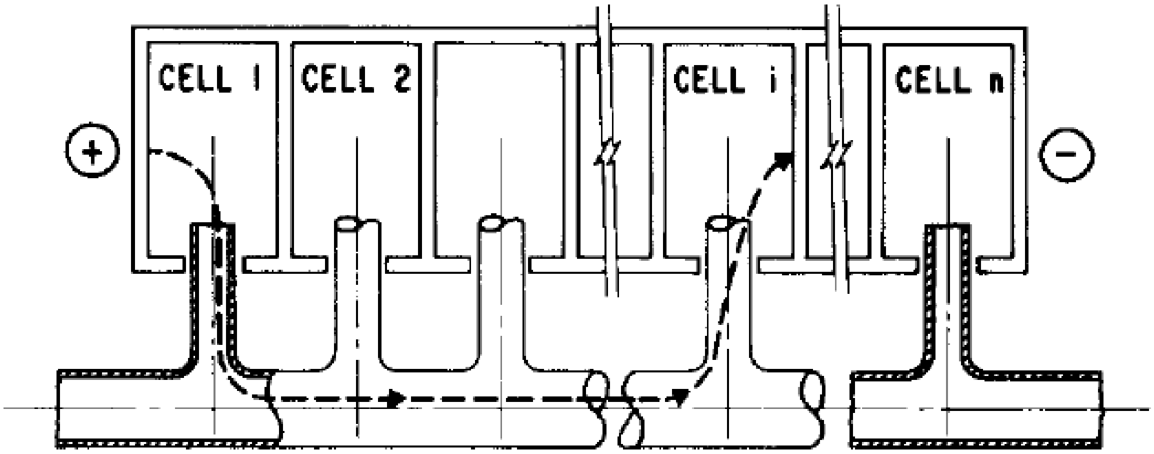

Figure 2.5: Schematic representation of how a shunt current flows via the manifold. For the sake of simplicity, only the feeder (inlet) manifold is shown. The header (exit) manifold can be represented equivalently [24].

Numerous studies provide suggestions on how to calculate the shunt currents in an electrolyzer stack. Refs. [25], for instance, suggest that the bypass current for a bipolar stack can be theoretically calculated. First, the sum of the individual potential difference for each cell in the stack is taken:

$$U_N = \sum_{k=1}^{k=N} U_k \tag{2.9}$$

Next, a linear current-voltage relationship is assumed for each cell in the stack, which gives:

$$U_N = \sum_{k=1}^{k=N} (U_0 + R_\mathrm{e} i_k) \tag{2.10}$$

where U_0 is the equilibrium potential, R_e is the cell resistance and i is the current. Furthermore, it was assumed that U_0 and R_e are equal for all cells, so that they can be excluded from the summation.

$$U_N = NU_0 + R_\mathrm{e} \sum_{k=1}^{k=N} i_k \tag{2.11}$$

This relation is compared to the theoretical potential when there is approximately no shunt current flowing:

$$NU_\mathrm{l} = NU_0 + NR_\mathrm{e} i_\mathrm{l} \tag{2.12}$$

The bypass current ratio gives an indication of the current portion that leaks through the manifolds and is defined as:

$$\psi = \frac{Ni_1 - \sum_{k=1}^{k=N} i_k}{Ni_1} \tag{2.13}$$

From Equation 2.11, 2.12, 2.13, an expression can be obtained to determine the bypass current from the current-voltage relationship. According to this paper, the bypass current in a stack can be calculated based on the bypass current in a single cell.

$$\psi = \frac{NU_1 - U_N}{NU_1 - NU_0} \tag{2.14}$$

Refs. [26], on the other hand, approached the electrochemical cell as an electrical network, as illustrated in Figure 2.6. Electrolyte pathways were considered as electrical resistances. However, compared to the channel resistance, the manifold resistances were assumed to be insignificant enough to be neglected. Individual resistors were calculated with Equation 2.1, where the channel dimensions are involved.

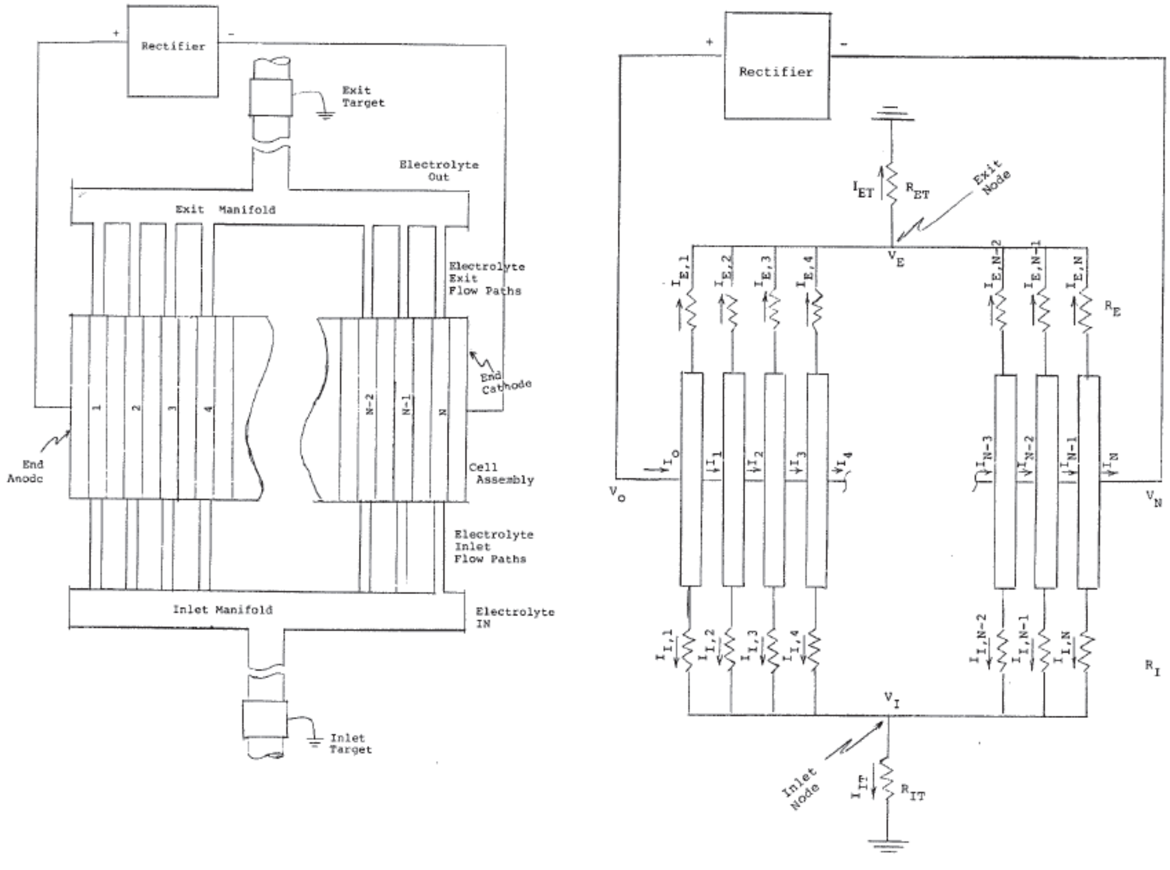

Figure 2.6: Equivalent electric circuit of an electrochemical cell assembly [26].

After simplifications of the resistance scheme, the following expression for the shunt current ratio was obtained:

$$\psi = \frac{\beta}{12}(N^2 - 1) \tag{2.15}$$

where β is the ratio of electrical resistance through the electrochemical cell to electrical resistance through the bypass conductive pathway. It gives an indication of how likely shunt currents will occur in a cell. N is the total number of cells, and it should be noted that the shunt ratio increases quadratically with N. More information on shunt current calculation and graphical representations of shunt currents in manifolds and cell channels is provided in Appendix B.

2.3. Bubble flow

During alkaline water electrolysis, bubbles are produced on the electrode surface. As a result, multiphase flow is present along the electrode surface and outlet manifolds. Therefore, it is necessary to comprehend the bubble behavior within a liquid. The mechanisms and flow regimes of bubbly flows will be covered in this section.

2.3.1. Bubble evolution and coalescence

There are two ways for bubbles to evolve [27]. In the first method, a single bubble detaches from the electrode surface, remains enclosed in the bubble layer, and continues to evolve as it diffuses into the bulk. In the second technique, a bubble that has separated and begun to ascend will collide with surrounding gas bubbles, enlarge even more and jump towards the bulk. The process by which bubbles coalesce consists of three steps. Firstly, two bubbles collide and trap a thin liquid layer between them. Second, the liquid film drains until it can no longer withstand the attractive forces between the bubbles. Finally, the bubbles will burst, coalesce, and subsequently larger bubbles will form. Coalescence will occur only if sufficient time is allowed for the film to drain to a critical thickness where bubbles can rupture. Refs. [28] assumed that in addition to the diffusion and coalescence regions, there is also an adherence region at the electrode surface, where bubbles are stuck or extremely close to the electrode surface. Typical bubble regions (e.g., coalesce, diffusion, and adherence) are illustrated in Figure 2.7.

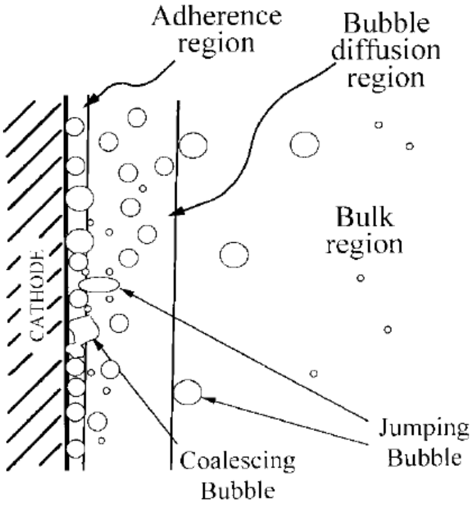

Figure 2.7: Bubble regions at the electrode surface [28].

2.3.2. Hydrodynamics

In electrochemical cells, bubbles are generally not desired due to their contribution to cell inefficiency. They take up space on the electrode surface, making it difficult for liquids to reach and pursue the reaction. However, bubbles can also enhance mass transport as a result of their hydrodynamic behavior. The effect of bubbles on hydrodynamics can be described by three models [28]. The first model is the penetration effect, in which a rising bubble leaves a mixing momentum (wake) behind in the flow, improving the mass transfer. The second model is the micro-convection effect, which occurs when a growing bubble pushes fluid in all directions around the electrode surface, resulting in a flow. Micro-convective flow dominates in stagnant flow (i.e., no forced circulation). The final model is the macro-convection effect, in which ascending bubbles encourage flow and improve mass transfer. Since mass and heat transport are often inextricably linked [29], bubbles also help remove heat from exothermic processes. Different bubble behaviors appear in laminar, turbulent, and buoyancy-driven flow regimes. [30]. Flow patterns of the different regimes in vertical cells are shown in Figure 2.8. It is expected that, by applying forced flow, bubbles will be swept from the surface faster, resulting in a smaller ohmic drop in a cell. Refs. [31] found that applying a flow had a large and positive impact on the cell voltage. Similarly, Refs. [32] observed experimentally that bubble coverage strongly decreases as vertical liquid flow velocity at vertically placed electrodes increases. Refs. [33] investigated the relation of cell voltage and flow rate for an electrolysis cell, containing a platinum anode and carbon cathode in a 8 M KOH solution. A drop in cell voltage of at least 150 mV was observed for current densities higher than 5 mA/cm^2 and flow rates of at least 1.5 mL/s. Nevertheless, Refs. [34] noticed small to no reduction in the ohmic drop in the cell containing nickel plates in 0.5 M KOH. It was observed that at current densities of 0.75 mA/cm^2 and 200 mA/cm^2, and a Reynolds number of 2521, bubble sizes were drastically reduced. However, the reduction in cell voltage was insignificant, due to the still existing gas layer on the electrode surface.

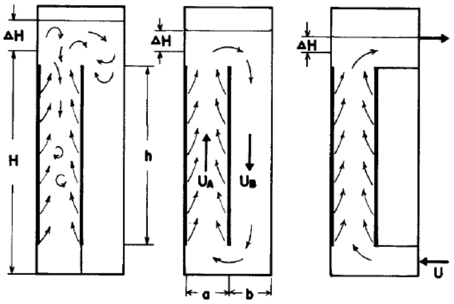

Figure 2.8: Flow pattern of different flow regimes in vertical cells; blocked convection on the left, free convection in the middle, and forced convection on the right [29].

2.3.3. Potential-current dependency

Bubbles reduce electrolyte conductivity, making it harder for hydroxide ions to travel through. Consequently, this will also lead to an increase in the ohmic resistance and an ohmic drop over the electrolyte. Increasing the cell voltage might encourage to overcome the bubble resistance, but there may be adverse effects.

The applied cell voltage has an impact on both bubble formation and dispersion. As the cell voltage increases, the current density also increases, and more bubbles will be generated at the electrode surface. The (normal) superficial gas velocity at which bubbles depart from the electrode surface at a given current density j, can be calculated using Equation 2.16 [35]. The superficial velocity is an artificial flow velocity that assumes that the given phase is the only one flowing or present.

$$u_{\mathrm{g}} = j\frac{V_{\mathrm{m}}}{nF} \tag{2.16}$$

where u_{g} is the superficial gas velocity, j is the current density and V_{m} is the molar volume.

At sufficiently high current densities, supersaturated electrolyte may form [36]. As a result of high supersaturation, the diffusion coefficients inside the gas layer will drop, causing dissolved gases to be transported away at a much slower rate. Consequently, heat, generated as a result of larger electrical resistances, will begin to accumulate, inducing an increase in temperature in the solution. However, there is a transition region in which the current density drops as the cell voltage increases further [36]. The higher cell voltage in this transition region will result in higher temperatures at the electrode-electrolyte interface. Once the temperature at the electrode surface reaches the boiling point of the water, evaporation of the water will begin at a constant temperature. Subsequently, the contact area between the electrode and the electrolyte will increase, resulting in a decrease in the current density. By increasing the potential even further, the transition region will fade into a “film electrolysis” region, in which the electrode is covered by a film of water vapor. Charge is transported by ions, and electrolysis takes place at the gas-liquid interface. Since the electrode is thermally isolated due to the gas layer, the temperature will rise by hundreds of degrees Celsius. The maximum current density for water electrolysis is therefore constrained by the occurrence of film electrolysis. However, this phenomenon will be less significant for vertically placed electrodes, because the electrolyte flow will force the bubbles away from the surface.

Ref. [34] investigated the bubble formation as a function of applied cell voltage in AWE. It was found that as the cell voltage increased, the critical diameter for detachment also increased. Furthermore, it was observed that as the cell voltage increased, the number of bubbles detaching also increased. However, the critical diameter decreased with the electrolyte concentration. Refs. [37] investigated the temperature in the bubble zone as a function of cell voltage. Temperature was observed to increase drastically when cell voltage also increased. The temperature measured on the electrode reached the boiling point of the electrolyte in the coalescence region.

2.4. Scaling for the channel resistance

In addition to providing a passage for hydrogen gases created in the cathodic chambers to escape, the outlet channels also allow hydroxide ions to pass through. Therefore, both the electrical resistance and the flow resistance are significantly influenced by the channel dimension.

A scaling for the electrical resistance can be derived using Equation 2.1. The channel is rectangular in shape, thus the cross-sectional area scales with the width w and height h of the channel. Equation 2.1 becomes:

$$R_{\text{electric}} = \frac{L}{w\,h\,\kappa} \tag{2.17}$$

where l is the length of the channel and κ is the electrical conductivity of the electrolyte flowing through the channel. When $w \approx h$, Equation 2.17 becomes:

$$R_{\text{electric}} = \frac{L}{h^2\,\kappa} \tag{2.18}$$

As the electric resistance and hydraulic resistance are analogous, the hydraulic resistance may be computed using Ohm's law for the electrical resistance. The pressure drop can represent the voltage drop, and the electrolyte flow rate can be used to represent the current flow, as shown in Equation 2.19

$$R_{\text{hydraulic}} = \frac{\Delta p}{\Delta Q} \tag{2.19}$$

The Hagen-Poiseuille equation is used to find an expression for the hydraulic resistance. The Hagen-Poiseuille equation can be derived from the Darcy-Weisbach equation [38], which is given by

$$\frac{\Delta p}{L} = f_{\text{d}}\,\frac{\rho}{2}\,\frac{u^2}{D_{\text{h}}} \tag{2.20}$$

where Δp is the pressure drop, f is the friction factor, ρ is the density, u is the flow velocity and D_{h} is the hydraulic diameter. For laminar flow in a circular pipe, the friction factor f is $\frac{64}{\text{Re}}$ where Re is the Reynolds number, which is equal to $\frac{\rho u D_h}{\mu}$. The electrolyte flow rate is given by

$$Q = \frac{\pi D_{\text{h}}^2}{4}\,u \tag{2.21}$$

Substituting Equation 2.21 into Equation 2.20 and eliminating u, the Hagen-Poiseuille equation is finally found.

$$\frac{\Delta p}{L} = \frac{128}{\pi}\,\frac{\mu Q}{D_{\text{h}}^4} \tag{2.22}$$

The hydraulic resistance then becomes

$$R_{\text{hydraulic}} = \frac{128}{\pi}\,\mu L\,\frac{w+h}{2wh} \tag{2.23}$$

The hydraulic diameter for a rectangular duct is defined as $\frac{2wh}{w+h}$. For the case where $w \approx h$, the hydraulic diameter scales with the channel height h:

$$R_{\text{hydraulic}} = \frac{128}{\pi}\,\frac{\mu L}{h^4} \tag{2.24}$$

It is desired to maximize the electrical resistance in order to reduce the shunt current, and to minimize the hydraulic resistance to increase the flow rate. However, as shown above, the channel dimensions contradict each other in terms of requirement. Equation 2.17 shows that if the channel height is decreased by a factor 2, the electrical resistance increases by a factor 4 while the hydraulic resistance increases by a factor 16.

3

Materials and Methods

This chapter outlines the upscaled electrolyzer design, components/supplies and the experimental procedures that were used.

3.1. Electrolyzer design

A larger and improved version of the zero-gap electrolyzer prototype, which was briefly mentioned in chapter 1, was developed to produce more hydrogen. A concise evaluation of the prototype is included in Appendix C. Initially, an electrolyzer stack was designed in SolidWorks as shown in Figure 3.1a. The electrolyzer is tightened with 18 M8 bolts and 6 M5 bolts. A single intake at the bottom allows the electrolyte to enter and simultaneously fill the cathodic and anodic compartments. Electrolysis occurs on the electrode surface inside the compartments. The gases created ascend and are guided through separate channels before exiting the electrolyzer, as shown in Figure 3.2a and 3.2b. Compared to the prototype, this design has a vacant space above the electrodes, which serves as a buffer zone for the bubbles to gather. The goal of this buffer zone is to avoid bubbles from covering the electrode surface. In addition, stainless steel plates were used as outer frames to distribute the compressive stress on the PMMA end plates more uniformly. To investigate channel clogging, a stack consisting of a single cell was used. An exploded view of a single cell is shown in Figure 3.3. The parts have numbers assigned to them, and the functions are outlined in Table 3.1.

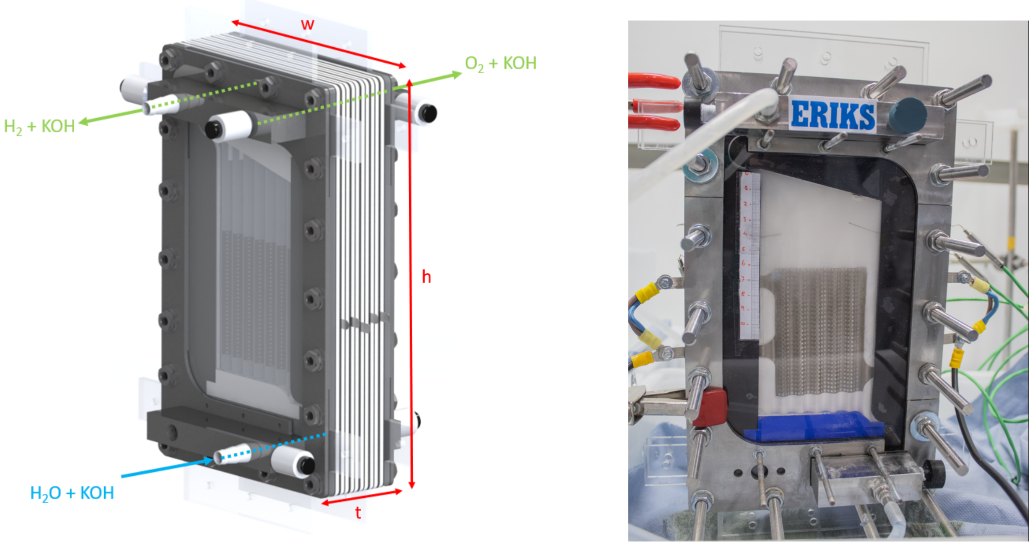

(a)

(b)

Figure 3.1: A rendering of the zero-gap electrolyzer stack containing 5 cells (a). The width w is 180 mm, the height h is 300 mm, and the thickness t is 65 mm. The manifolds are shown as dotted lines. Electrolysis takes place inside the compartments where the electrodes are located. The built electrolyzer containing a single cell is shown in (b).

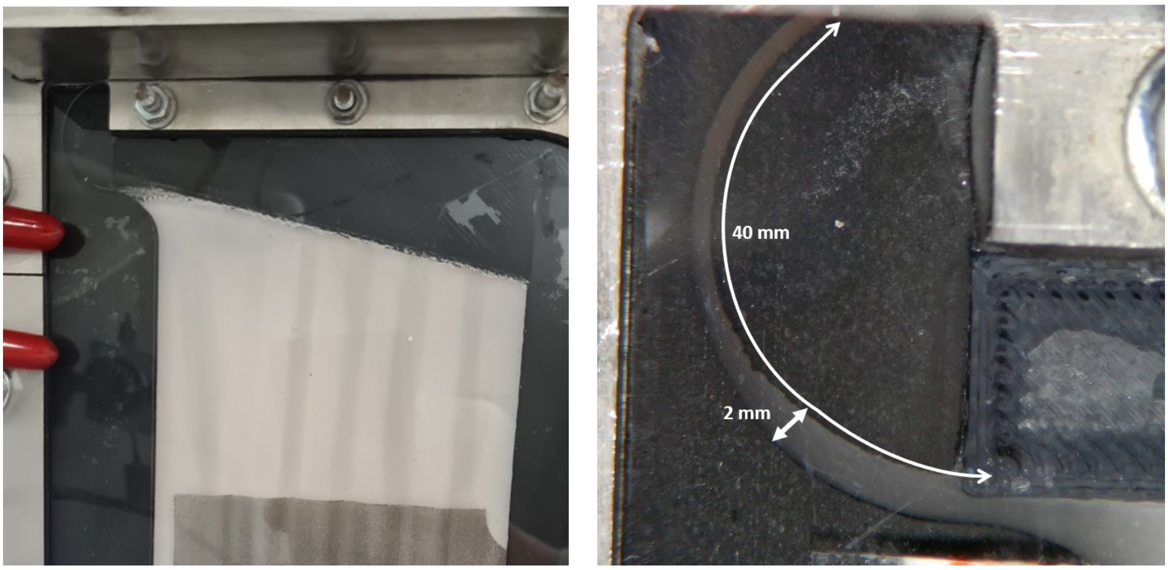

(a)

(b)

Figure 3.2: Top section of the cathodic chamber showing the slanted clamping block (a). The slanted clamping block directs the bubbles and electrolyte toward the exit channel at an angle of 13 degrees (b). The channel is 2 mm high, 3 mm deep and 40 mm long.

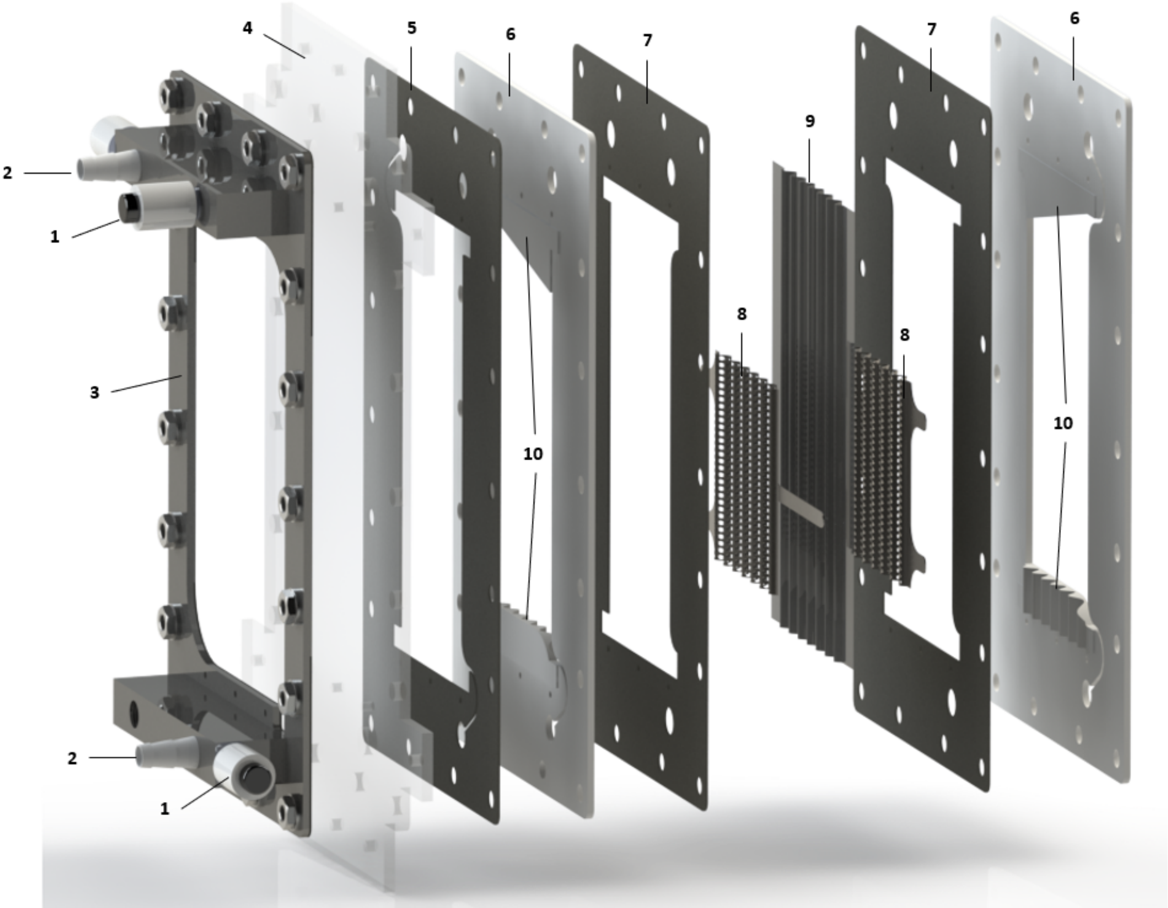

Figure 3.3: Exploded view of a single cell. The parts until the electrode (number 8) are in mirrored order after the diaphragm (number 9).

Table 3.1: Description of electrolyzer components.

Number	Component name	Function
1	Reference electrode	Measures the potential of the electrolyte at each manifold side.
2	Hose connector	Connects hose to manifold inlet/outlet.
3	Stainless steel (SS) frame	Provides homogeneous clamping pressure over PMMA endplate. SS is chosen due to its resistance to KOH and high yield strength.
4	PMMA endplate	Closes the stack externally. Provides possibility to visualize the generated bubbles inside compartments.
5	Viton™ Gasket	Forms sealing between PMMA endplate (4) and PMMA plate (6). Provides ability to visualize the bubble transport in channels.
6	PMMA plate cell	Provides a compartment for cathode/anode.
7	Viton™ Gasket	Sealing between PMMA plate (6) and electrodes (8).
8	Electrode	Electrical conductor that makes contact with electrolyte in order to perform electrolysis.
9	Zirfon Perl Membrane	Separates produced gases in the compartments. Sandwiched by the electrodes (8) and gaskets (7).
10	Slanted clamping block from 3D-printed ABS	Clamps the membrane (9) in order to prevent deformation due to flow during electrolysis. Secondary, it leads the gas bubbles towards the outlet channel of the compartment.

The electrolyzer was also designed so that the reference electrodes can be mounted on the ends of the manifolds. To reduce interference from bubbles in the flow that may affect the signal, we positioned the holes for the reference electrodes perpendicular to the ends of the manifold and crosswise at the inlet and outlet of the manifold. The difference in potential between these two reference electrodes can be measured with a voltmeter, which subsequently can be calculated into a (shunt) current via Ohm's law. Therefore, two reference electrodes are supposed to be between the end points of each manifold. An illustration of the location of the reference electrodes is provided in Figure 3.4. The inlet manifold is displayed at the bottom and the hydrogen manifold at the top. The black arrows indicate the flow directions inside the manifolds. The red arrows illustrate the possible pathways for the shunt current. The orange boxes represent the reference electrodes.

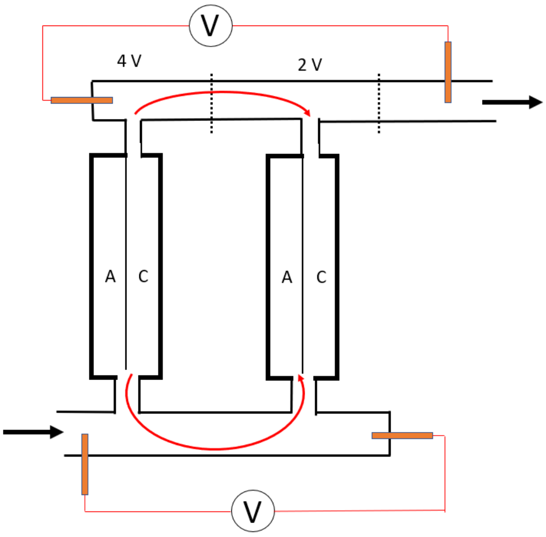

Figure 3.4: Schematic of the reference electrode locations in a dual celled stack. The oxygen manifold, which would likewise be at top, can be depicted similarly in a schematic.

3.2. Electrodes

Five electrode types were investigated in our research. The types are listed below.

1. In the initial stage, we used electrodes with a perforated shape. The electrodes were laser cut from a 0.5 mm thick stainless steel plate of type 304.
2. Next, a change was made to a 316 SS-woven mesh to observe the performance of an alternative electrode structure.
3. Subsequently, the SS-perforated plates and SS-meshes received nickel treatment for further investigation of the electrode performance with surface treatment. Electrodeposition was used by Haveman B.V. to apply a 6 micron thick nickel coating to the surface. It is expected that the treatment will merely change the activation regime, leaving the electrical conductivity unchanged.
4. Finally, similar to the SS-plate, a nickel plate electrode was laser cut from a 0.5 mm thick 201-type nickel plate. These electrodes had two flaps sticking out instead of only one flap compared to the previous electrodes. The initial run used only one flap that was electrically connected. A second run was performed with the two flaps interconnected by a copper wire, creating two parallel electrical connections to reduce the ohmic resistance.

The perforated shape was achieved by laser cutting small holes in the electrode. After laser cutting, all plate electrodes received a polish treatment with a #80 SiC foil from Struers. The flat shape of a (nickel) plate electrode with 2 flaps is shown in Figure 3.6. Subsequently, the flat electrode plates were sandwiched between 3D printed molds. The electrodes were given their final waved form by pressing the molds together using a vice. Figure 3.7 demonstrates how an electrode acquired its corrugated form. The waved design increased the electrode surface area to volume ratio approximately by a factor of 1.25. The wide flap that sticks out forms the electrical connection of the electrode.

All electrodes, except for the test cell, had equal shapes and therefore the same geometric surface area. A single electrode had a geometric surface area of $8\text{ cm} \times 9\text{ cm} = 72\text{ cm}^2$ that contributed to the electrolytic reaction. The electrodes in the electrolyzer were placed in an almost-zero-gap configuration. As the electrodes did not exactly fit together, the distance between them fluctuated locally between 2 and 4 mm.

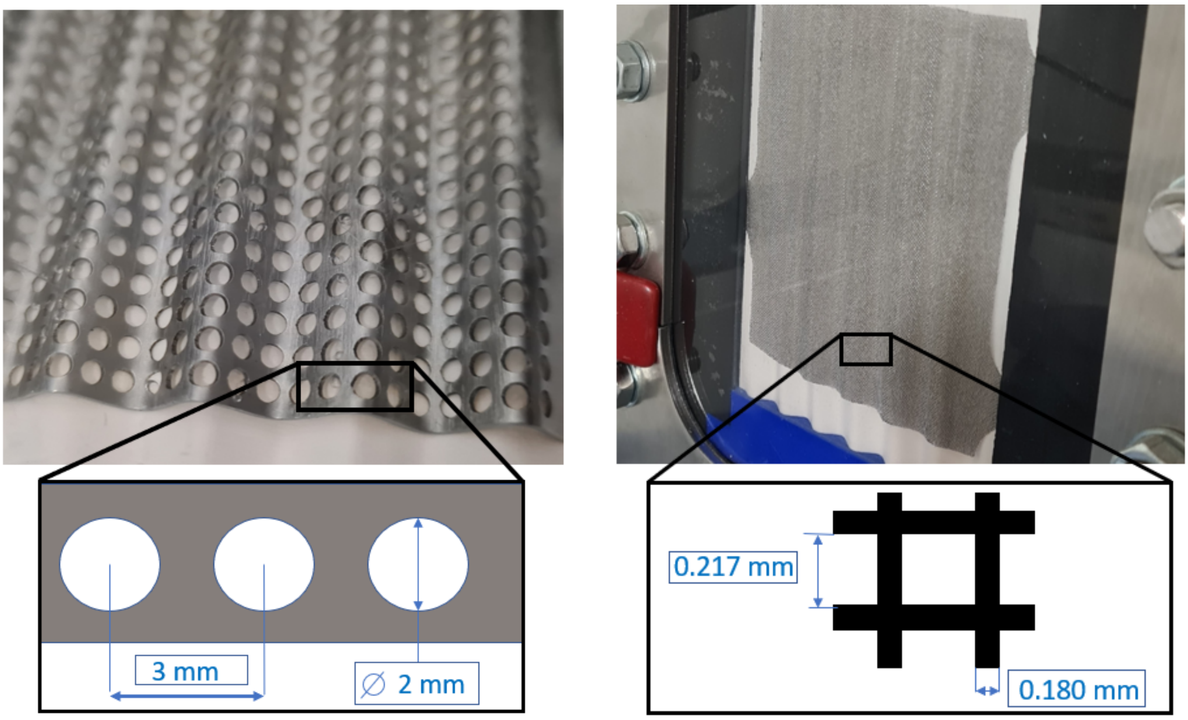

(a) (b)

Figure 3.5: The hole pattern in (a) the laser cut electrode from a 304 stainless steel plate and (b) the 316 stainless steel mesh.

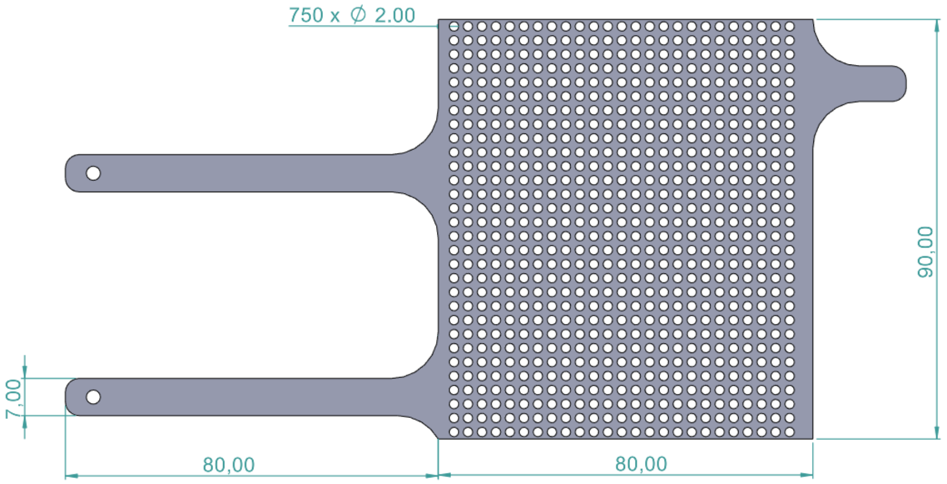

Figure 3.6: Electrode design with 2 flaps. The small holes in the flaps are connection points for electric leads with ring terminals. Dimensions are in mm.

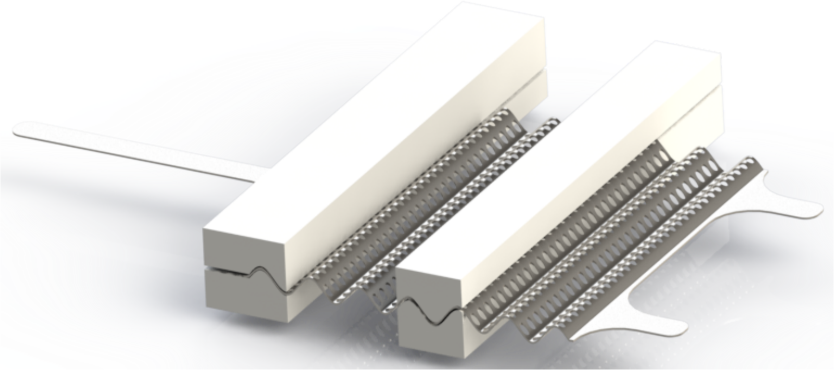

Figure 3.7: Electrode shaping with 3D-printed molds.

3.3. Equipment and experimental setup

KOH electrolyte was prepared with KOH pellets and milli-Q water. The KOH pellets used were from Sigma Aldrich$^{\text{TM}}$ which have a $\geq$85% purity rating. Because the preparation of a KOH solution involves an exothermic process, a batch of electrolyte was prepared at least one day in advance of the experiments. Electrolyte at room temperature and with a concentration of 6M was used for all experiments.

The thermocouples that were used were Type K. A single thermocouple was immersed in the electrolyte reservoir and 4 thermocouples were installed on the single cell electrolyzer stack. Two of these thermocouples were installed on the cathode side, whereas the other two were installed on the anode sides of the compartments, one on each side. The probes in the electrolyzer were placed exactly above the electrodes because the reaction heat was carried away vertically. The 0.5 mm diameter and 100 mm long probes allowed them to be sandwiched between two gaskets that faced each other (as numbers 7 in Figure 3.3).

A PUMPDRIVE PD5006 Heidolph peristaltic pumping device was used to pump the electrolyte through the electrolyzer. The average flow rate was measured experimentally. The electrolyte was pumped into the electrolyzer, and the liquid level was monitored with the high-speed camera. Since the liquid flow velocity in the compartment was known, the flow rate was calculated by multiplying the liquid velocity, which is in our case equal to the superficial liquid velocity, by the flow-through area. This was done on both sides of the electrolyzer.

A Delta Elektronika SM 15-200 D power supply was used to regulate the potential. The voltage was measured with a Plieger Basic multimeter with an accuracy of 0.01 V. To measure the current, a VC-330 AC/DC miniclamp meter was used. The accuracy of the clamp meter was 0.01 A.

A microscope camera was used to capture the bubble distribution. The microscope camera employed was a 38 MP FHD Camera V6 with a mounted microscope objective that can go up to a magnification of 100x. In

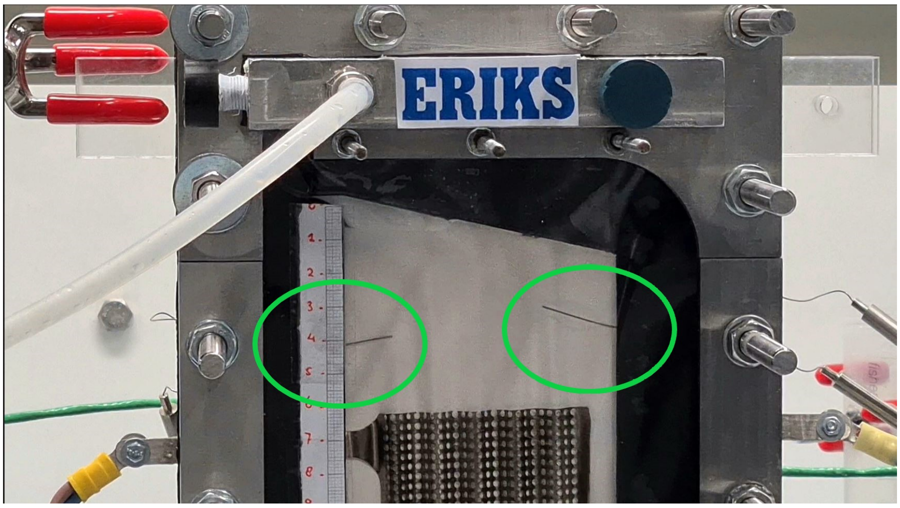

Figure 3.8: The cathodic side of the electrolyzer with thermocouples attached from the sides. The probes (illustrated with green circles) reach the compartments inside the electrolyzer cell. The left probe was at the outlet side of the compartment.

addition, a 1 MP Nova Fastcam series by Photron camera was used to capture high speed videos of the moving bubble layer. The camera was equipped with a 1:1 macro lens with a 105-mm focal length and an f/2.8 maximum aperture. The 950 lumen Brennenstuhl LED panel was utilized to illuminate the bubbles.

The H_2 and O_2 gases formed were separated from the electrolyte by self-made gas-liquid separators before the gases were released into the atmosphere. The gas-liquid separators were made from a syringe without a cap. A hole was drilled from the side where gas and liquid from the electrolyzer could enter. Another hole was drilled at the bottom of the syringe where the liquid could flow back to the reservoir. Each electrolyzer outlet was directly connected to the gas-liquid separator by silicon hoses. The experiments were performed inside a fume hood where the gases were released. The gas-liquid separators were placed 0.5 m from each other to minimize the risk of gaseous mixtures. It was calculated that at a current density of j = 400 mA/cm^2, the hydrogen production would be approximately 10 Liters per hour. Because hydrogen is a lighter gas, it would be sucked up by the ventilation system of the fume hood. A picture of the setup inside the fume hood is shown in Figure 3.9 and a schematic view is provided in Figure 3.10.

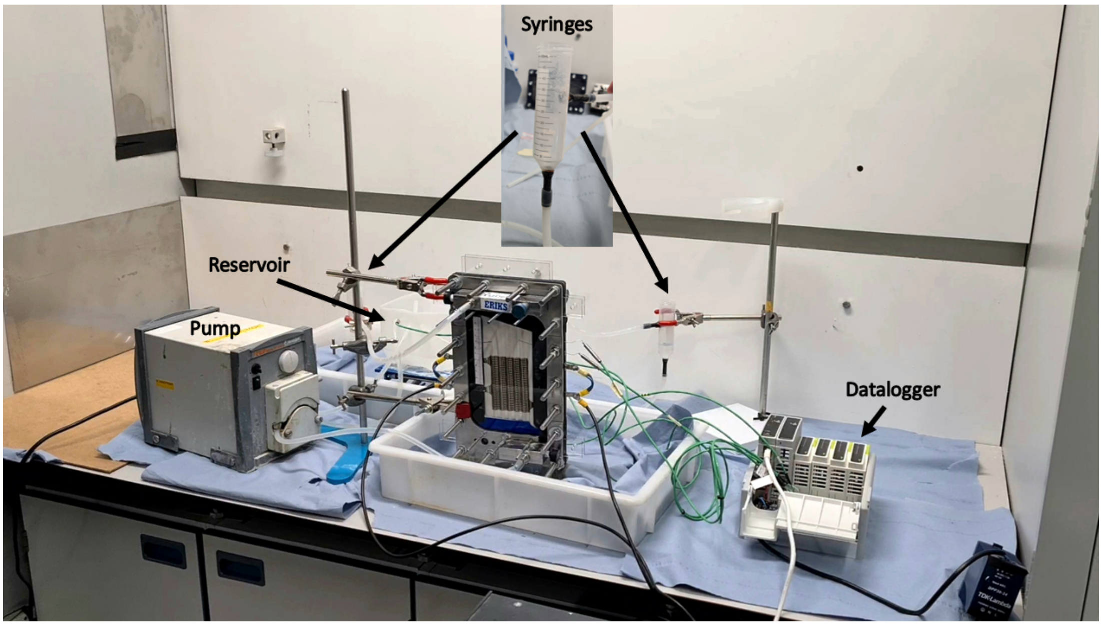

Figure 3.9: The experimental setup inside the fume hood. The electrolyte reservoir can be seen in the background. The syringes affixed on the stands serve as the gas liquid separator. The electrolyzer is shown on the foreground.

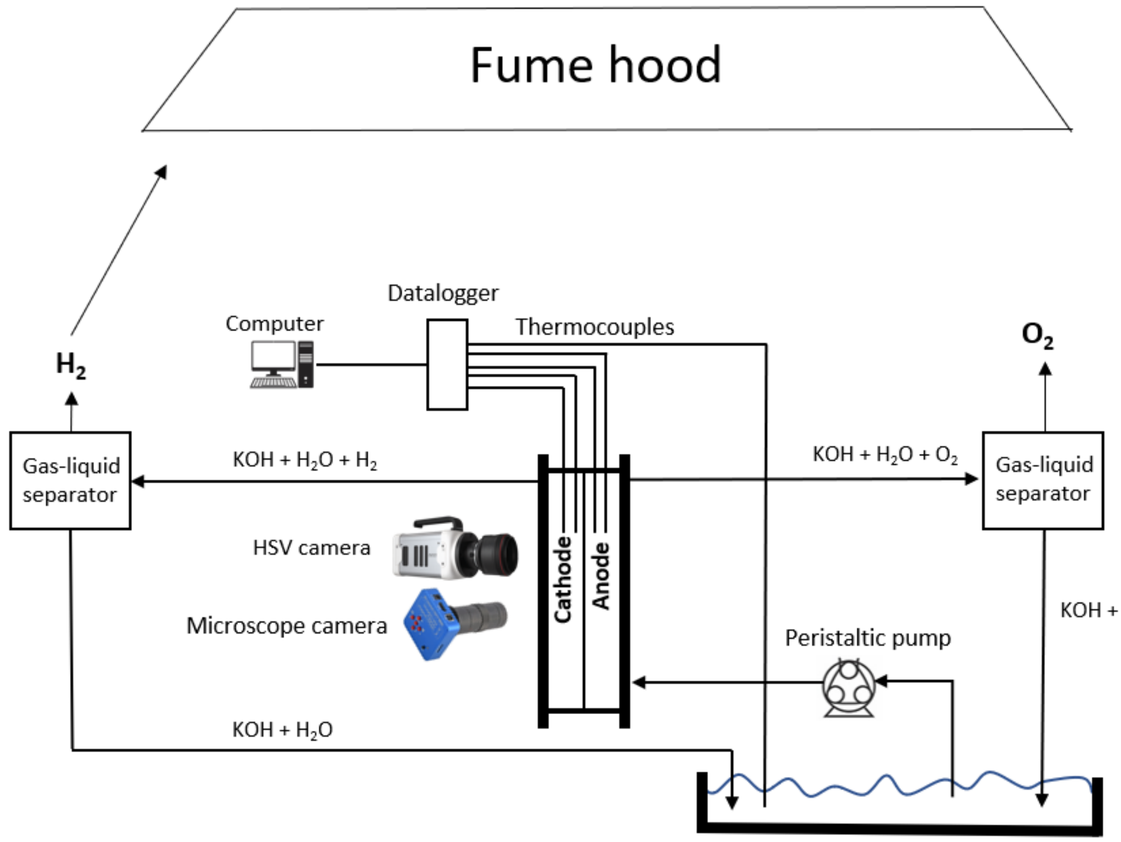

Figure 3.10: Schematic of the single-intake and single-cell electrolyzer in the intended electrolysis setup that is shown in Figure 3.9.

3.4. Characterization

Experiments were conducted to characterize electrochemical behavior, as well as flow at atmospheric pressure, room temperature, and with 6M KOH electrolyte.

3.4.1. Electrochemical

The characterization of the performance of the electrolyzer is determined by performing an *I-V* test. During this test, a potential difference was applied by a power source between the electrodes. A voltage of 1.50 V, which is roughly the thermoneutral voltage, was applied initially and gradually increased with increments of 0.05 V until higher current densities were achieved. The highest applied current density was 450 mA/cm^2, which, for the given electrode surface areas, corresponds to a total current of approximately 32.4 A. While the applied potential was measured with a voltmeter, the current was simultaneously measured with an ammeter. IV curves were obtained for various electrode materials and shapes. Tafel slopes for the different electrodes were then calculated and listed in a table.

3.4.2. Flow

The channel blockages only took place at the cathode side. As a result, a high-speed camera and a microscopic camera were used to capture videos only on this side. Subsequently, the video frames were qualitatively analyzed with image processing tools to characterize the flow. When clogging occurred, the video frames,as shown in Figure 1.3, were analyzed for flow characterization based on the following three parameters: :

- The bubble size distribution.
- Average velocity of the bubble layer at the slanted top.
- Flow regime in which clogging occurs.

Bubble size distribution

Finding the bubble size distribution is necessary since it will reveal how the bubbles are scattered when channel congestion occurs. For this purpose, only the bubbles at the tilted top of the electrolyzer were subjected to inspection. This is because during the operation, a large number of hydrogen bubbles were created in the compartment, which caused the electrolyte to become highly cloudy around the electrode surface. The microscope videos were captured with a frame rate of 60 frames per second and in Full High Definition (FHD) resolution. The videos were taken at a distance of approximately 10 cm from the PMMA end plate using the microscope. Due to limitations of the camera lens, only bubbles with diameter greater than 0.15 mm were taken into consideration. The video viewer function in Matlab was used to inspect the recorded videos frame by frame. Frames were selected based on the sharpness and the moment at which the clogging occurred. The chosen frames were then further analyzed with the image processing program ImageJ in which all bubbles were encircled manually. The script output was a matrix with the x-y coordinates and the radii of the identified bubbles, all measured in pixel units. The pixels were then converted into metric units of length with a conversion factor. A scale, which was printed and attached to the PMMA end plate, was used to calculate the conversion factor. One pixel equaled 0.0216 mm. The bubble diameter distribution plots were then generated using the data collected from ImageJ.

Bubble layer thickness and velocity

The velocity and thickness of the bubble layer provide valuable information on the probability of clogging. Understanding how the bubble layer develops and how different flow rates affect it is crucial. The peristaltic pump's rpm knob is used to adjust the flow rate. To determine the velocity of the bubble layer, a high-speed video (HSV) was captured. These video frames were used to divide the distance traveled by a single bubble by the time it took to reach its destination. Figure 3.11 shows an example of a single bubble tracked. The thickness of the bubble layer was measured using ImageJ software, which converts pixels to absolute length. The thickest point of the bubble layer, which is close to the outlet channel, was measured as shown in Figure 3.11a. The HSV was captured using a 1 MP high-speed camera at 125 fps at a distance of approximately 30 cm from the PMMA end plate. One pixel equaled 0.081 mm.

In addition, thermocouples were used to monitor the liquid temperature and assess the difference in flow rate between the anodic and cathodic compartments without using flow meters. Significant temperature differences between the anode and cathode indicate that the electrolyte may prefer to flow through one of the compartments.

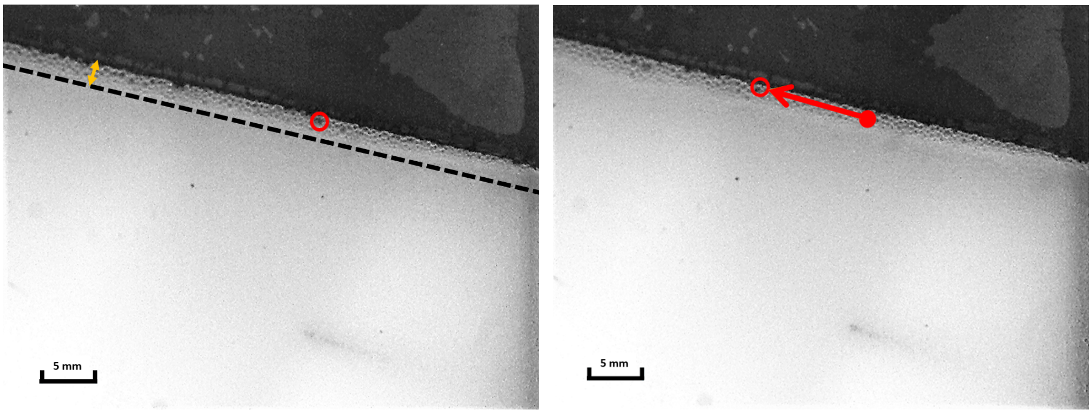

(a) t = 0 s **(b)** t = 0.2 s

Figure 3.11: (a) Maximum hydrogen bubble layer thickness indicated with a yellow arrow and the initial state of a bubble being tracked (red circle) and (b) the displacement (indicated as a red arrow) relative to the initial state at different time points.

Slug flow regime

To map the conditions in which blockages occur, it was essential to identify the flow regimes in which clogging takes place. The key parameters in this experiment were the superficial liquid and gas velocities. To vary the superficial gas velocity, and thereby the current density, which is directly proportional to the gas velocity, the current density was changed during the experiments, as shown in Equation 2.16. Before each run, the superficial liquid velocity was adjusted by varying the pump flow rate. The current density was gradually increased until no clogging was visually observed. At this point, the corresponding parameter values were recorded, and a plot was generated, with the superficial gas velocity plotted against the superficial liquid velocity.

4

Results

4.1. Electrolyzer characteristics

Figure 4.1 shows the *j*-*V* data points for several electrode materials. The graph shows what the voltage is for a given current density. The fitted curves are made using Equation 2.8 as a custom equation in Matlab.

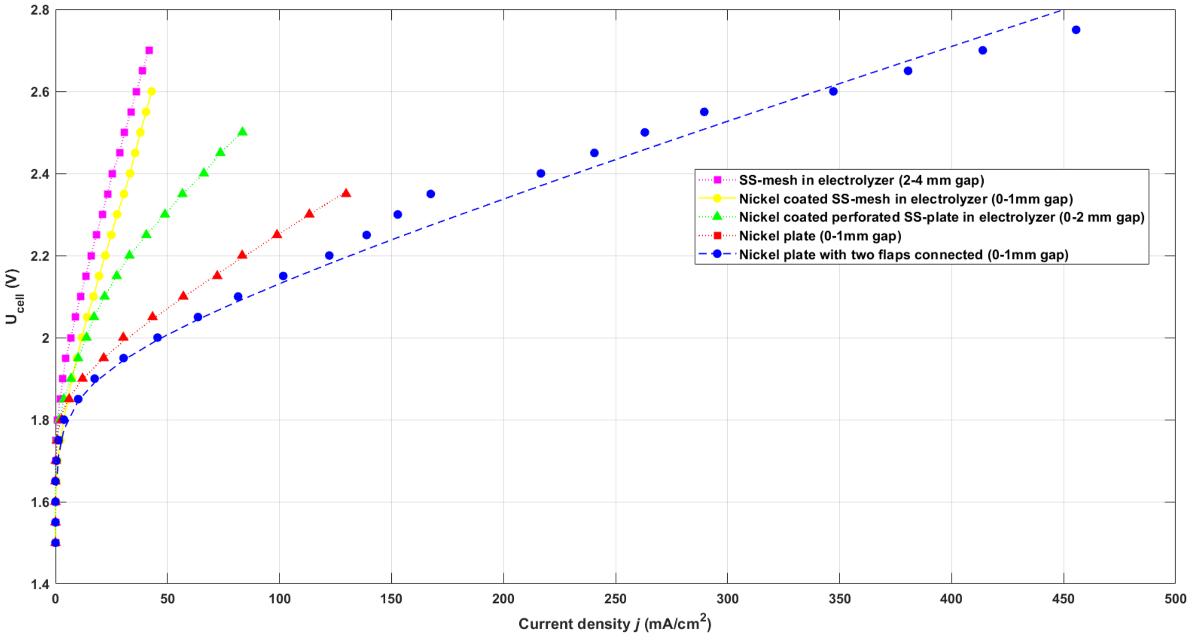

Figure 4.1: Selected *j*-*V*-curves of the electrolyzer for several electrode materials. The experiments were performed at room temperature, atmospheric pressure and with 6M KOH. The lines represent the fits made with Matlab.

The steep slope of the meshes in the electrolyzer indicates a higher ohmic resistance compared to other structures. The nickel-coated SS-mesh shows a vertical shift in the curve but with an unchanged slope, which is expected. On the other hand, the nickel-coated SS-plate exhibits improved conductivity compared to the SS-mesh due to the increased electrode thickness, resulting in reduced electrical resistance. The use of a nickel plate electrode, which has material characteristics superior to those of stainless steel, shows a smaller slope. Moreover, interconnecting the two flaps of the nickel plate with copper wires results in a further decline in slope, indicating the significant role of ohmic resistance in the current distribution across the electrode surface.

Equation 2.8 was used to determine the exchange current density j_0, the Tafel slope b, and the ohmic resistance R for the electrode configurations. Table 4.1 shows the coefficients for the different configurations.

According to Table 4.1, a mesh electrode exhibits a higher resistance than a plate electrode with identical shape dimensions. This is likely due to poor surface contact between the woven strands in a mesh, which leads to higher contact resistance. Furthermore, an increase in electrode dimensions results in a significant increase in

Table 4.1: Parameters for different electrode materials. j_0 is the exchange current density, b is the Tafel slope, R is the ohmic resistance and R-square is the proportion of the variance of the fit.

Electrode	j_0 (A/cm^2)	b (mV/dec)	R (Ω cm^2)	R-square
SS-mesh	0.035	210	17.86	0.9961
SS-mesh Nickel coated	0.025	170	17.36	0.9982
Laser cut SS-plate nickel coated	0.017	180	5.992	0.9952
Laser cut nickel plate	0.0165	170	3.105	0.993
Laser cut nickel plate with two flaps interconnected	0.03	170	1.522	0.9837

resistance for woven meshes. This happens because electrons must travel a longer distance. Additionally, a long flap that serves as an electrical connection point contributes significantly to the total resistance of the system. The total resistance for a single flapped nickel plate electrode can be seen in Table 4.2, which was obtained using Equation 2.1. The table shows that the ohmic resistance for a woven mesh is approximately 3 times larger compared to a plate structure. It can also be seen that the 6 micron nickel coating reduces the Tafel slope by approximately 40 mV/dec, while the ohmic resistance remains the same. The difference in tafel slope between a nickel-coated electrode and a nickel-coated SS-plate is approximately 10 mV/dec, which might be attributed to inacurate laser cut meshes. It is plausible that the meshes were warped during laser cutting, resulting in a laser cut that was not exactly the intended shape. Finally, the table shows a difference in ohmic resistance when a second flap is connected to the first one by a copper wire. The overall resistance was reduced by a factor of 2, suggesting that the design of the electrodes has a significant impact on the total ohmic resistance. More flaps would likely further decrease the ohmic resistance at the expense of adding additional (valuable) components to the electrolyzer assembly.

The total resistance of a single electrode can be divided into two components, namely the flap resistance and the reactive electrode surface resistance. The calculations were performed under the assumption that the current is uniformly distributed over the reactive electrode surface. The proportion of the component resistance is presented in Table 4.2.

Table 4.2: Calculation of the ohmic resistance for the flap and the reactive surface of a nickel plate electrode. The flap occupies a large part of the total resistance of the electrode.

	Flap			Reactive surface electrode	
	Dimension	Units		Dimension	Units
Thickness	0.5	mm		0.5	mm
Length	80	mm		80	mm
Height	7	mm		90	mm
Electrical resistivity	8.5×10^{-8}	Ω m		8.5×10^{-8}	Ω m
Porosity	0	(-)		0.5	(-)
Resistance	1.94×10^{-3}	Ω		4.74×10^{-4}	Ω
Total resistance	2.37×10^{-3} Ω				
Percentage of total resistance	81.9 %			18.1%	

From the calculated electrode resistance values it can be inferred that a considerable portion of the total resistance is caused by the long flap, which accounts for the steep slopes in the ohmic regions of all electrodes.

4.2. Flow characteristics

This section will cover the results of the experiments to characterize the flow during clogging. We will first look at the bubble size distribution when clogging occurs.

Bubble size distribution

During clogging, the bubbles were captured and their sizes and distributions were evaluated. To get a bubble size distribution, we encircled the bubbles manually with ImageJ. The result of bubble encirclement is shown Figure 4.2a and Figure 4.2b when clogging was expected to occur at 17.5 mA/cm^2 and 45.6 mA/cm^2 respectively.

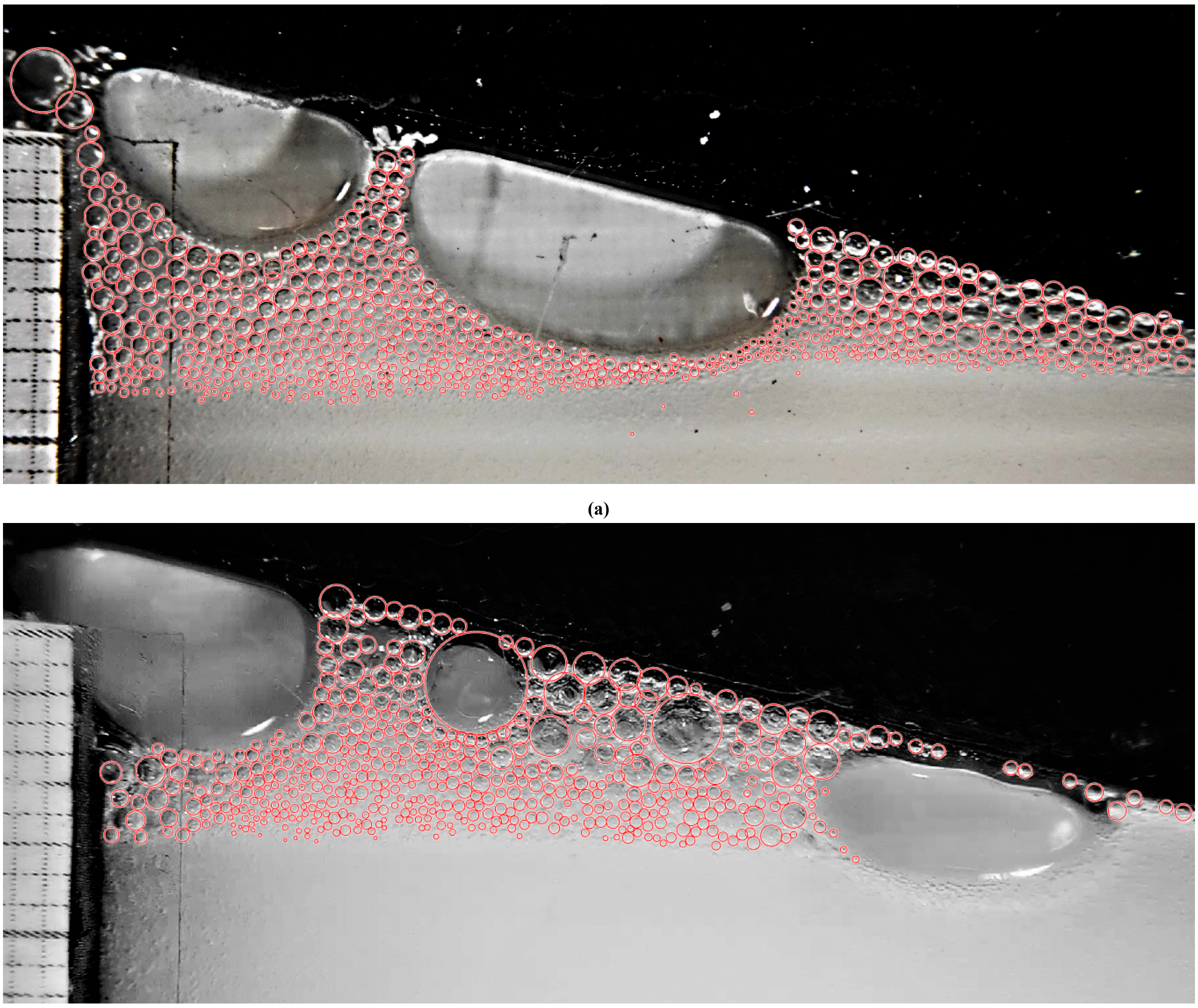

(a)

(b)

Figure 4.2: Encirclement of bubbles when blockage of the channel occurs at (a) j = 17.5 mA/cm^2 and (b) at j = 45.6 mA/cm^2. The flow rate is 1.6 ml/s. The bubbles are encircled manually with ImageJ. The size of the larger uncircled bubbles are more than three times the height of the channel.

The larger bubbles, which eventually led to the restriction of the exit channel, were not encircled because they make the distribution wider and more obscure. The scale on the left side of the figures indicates that the sizes of these large bubbles are approximately three times the channel height. The encircled bubbles of both images are translated into bubble size distributions, which are shown in Figure 4.3 and Figure 4.4 respectively.

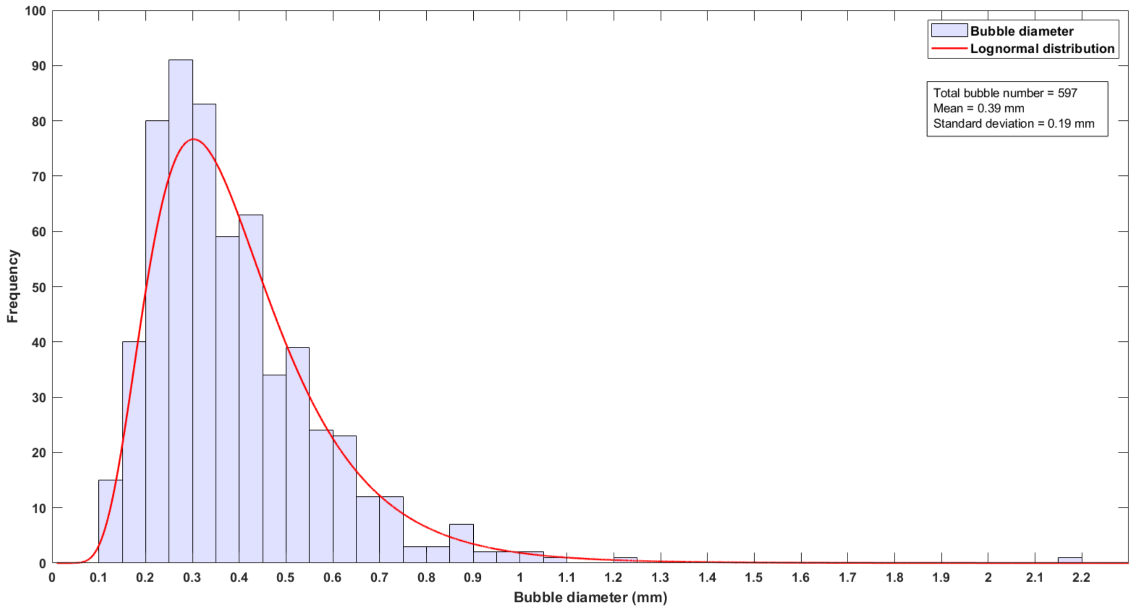

Figure 4.3: The bubble size distribution that belongs to Figure 4.2a. Current density j = 17.5 mA/cm^2 at a flow rate of 1.6 mL/s. The fit follows a lognormal distribution.

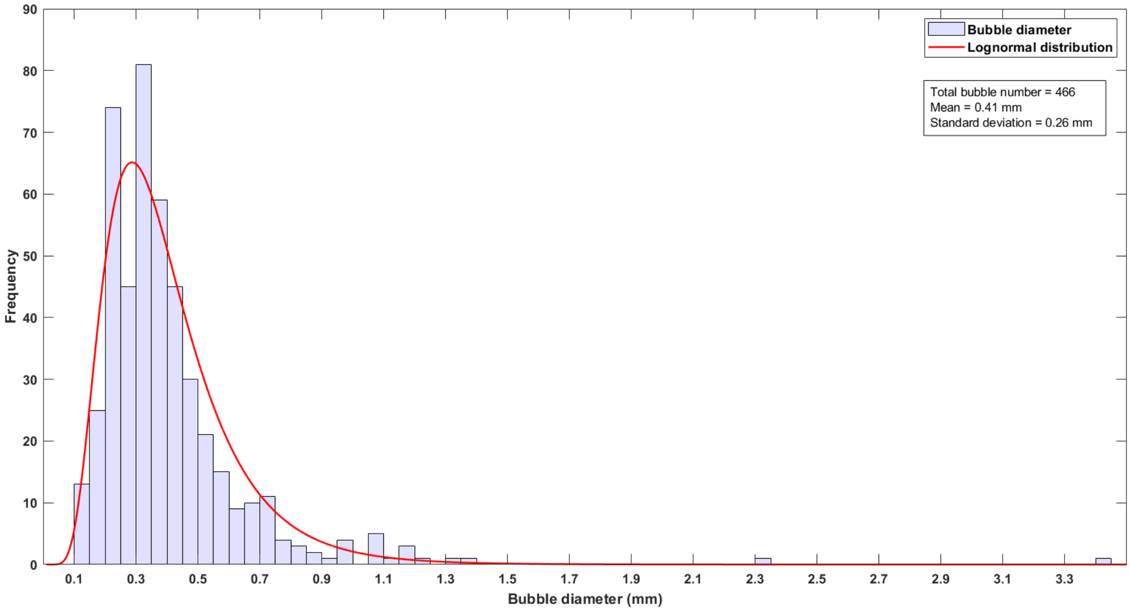

Figure 4.4: The bubble size distribution that belongs to Figure 4.2b. Current density j = 45.6 mA/cm^2 at a flow rate of 1.6 mL/s. The fit follows a lognormal distribution.

The graphs reveal that the distributions are skewed to the right and the bulk of the data is concentrated around the mean of the logarithm of the bubble sizes, which is typically described by a lognormal distribution as shown in Equation 4.1 [39].

$$y = f(x|\mu,\sigma) = \frac{1}{x\sigma\sqrt{2\pi}} \exp\left\{ \frac{-(\log x - \mu)^2}{2\sigma^2} \right\}. \tag{4.1}$$

where x is the diameter of the bubble, μ is the mean of the logarithmic value and σ is the standard deviation of the logarithmic values.

μ and σ can be calculated with the mean m and variance v of the distribution:

$$\begin{aligned}\mu &= \log\left(\frac{m^2}{\sqrt{m^2+v}}\right)\\ \sigma &= \sqrt{\log\left(\frac{v}{m^2}+1\right)}\end{aligned} \tag{4.2}$$

The fit parameters for the two distributions shown above are given in Table 4.3. According to the fitted curve, the absolute mean size of the bubbles was about 0.4 mm at the point of channel blockage. This mean bubble size is 5 times smaller than the channel height, which was 2 mm. However, certain extremely high values that exceed the channel height also appear. To clarify what the volume occupied by these large bubbles is, the volume fraction distributions that belong to the bubble size distributions are provided, respectively, in Figure 4.5 and Figure 4.6.

Table 4.3: Coefficients of Equation 4.1 for the bubble size distributions shown in Figure 4.3 and Figure 4.4.

Distribution for j (mA/cm^2)	Number of detected bubbles	μ	σ
17.5	597	-1.047	0.438
45.6	465	-1.021	0.476

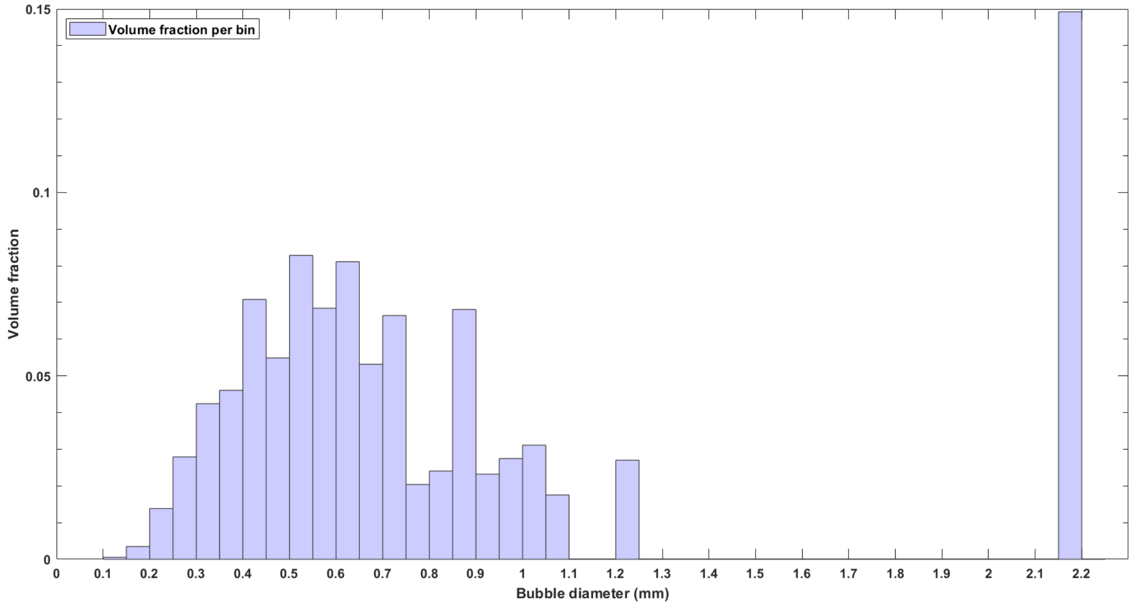

Figure 4.5: The volume fraction distribution of Figure 4.2a as a function of bubble diameter. The volume fractions are relative to total volume of the bubbles. Current density j = 17.5 mA/cm^2 at a flow rate of 1.6 mL/s.

It can be seen that large but irregular bubbles occupy approximately 15 to 40% of the total bubble volume present in the bubble layer. Bins on the left side typically have volume fractions that are no higher than 0.06. With the bubble volume fraction quantified, we now explore the bubble size distribution as a function of height. As shown in Figure 4.2a and 4.2b, the bubble layers are triangular in shape. This triangle is divided into four vertical zones of equal heights, as depicted in Figure 4.7 for further analysis of the bubble distribution.

The height of each region is specified relative to the thickness of the bubble layer. Figure 4.8 shows the bubble size distribution per region for Figure 4.2a. The y-axis gives the percentage of the bubble range that is present in the respective region. As can be observed, the lowest zone often has the smaller bubbles, and as we move upward through the zones, larger but fewer gas bubbles are present. The graph also demonstrates that bubbles with diameters less than 0.40 mm are typically found in the bottom section, but are absent in the top. The upper areas are mostly crowded with bubbles ranging in size from 0.40 to 0.60 mm. A similar trend is found when we look at Figure 4.9 which shows the bubble size distribution as a function of height for Figure 4.2b. which is. The bottom region contains mainly bubbles that are smaller than 0.40 mm, whereas the bubbles increase in size as we get to higher regions. The top region now contains more bubbles that are larger than 0.70 mm.

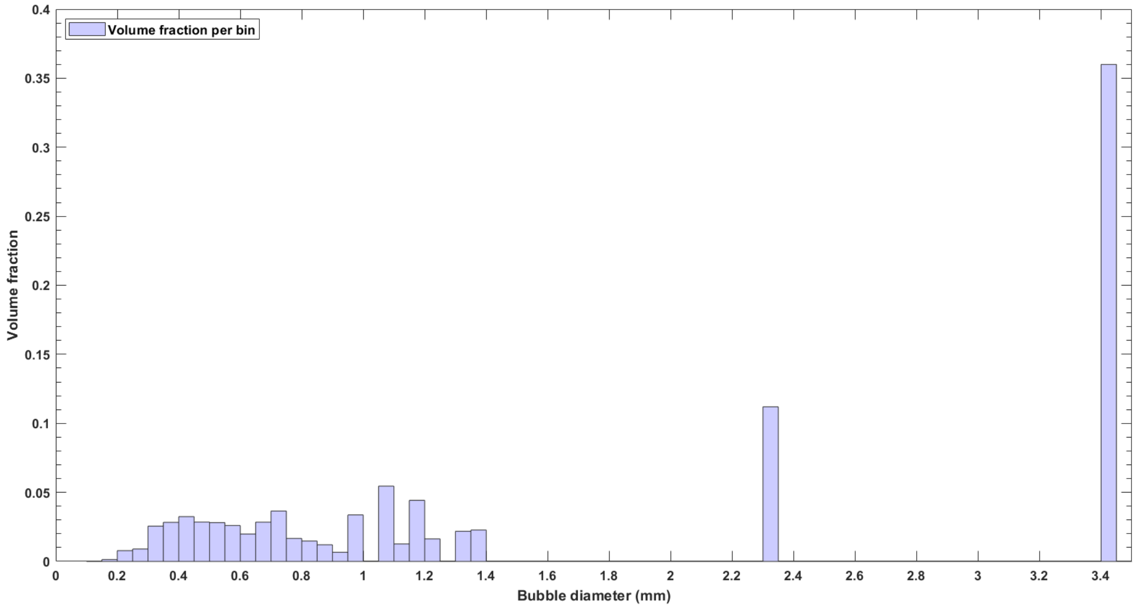

Figure 4.6: The volume fraction distribution of Figure 4.2b as a function of bubble diameter. The volume fractions are relative to total volume of the bubbles. Current density *j* = 45.6 mA/cm^2 at a flow rate of 1.6 mL/s.

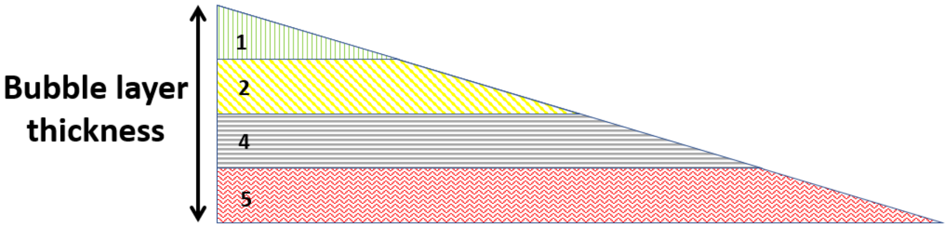

Figure 4.7: Illustration of subdivided zones in the bubble layer.

On the basis of the distribution of the bubbles and their sizes, we may conclude that the rising bubbles from the electrode surface are smaller than the channel height, which suggests that it is less likely that these bubbles might have clogged the channel if the larger bubbles were absent. Small bubbles are less likely to cause clogging than larger bubbles because they are more easily transported by the flow of the liquid. However, if small bubbles are dispersed at high concentrations, they can still cause clogging by accumulating and sticking together, forming larger bubbles that can block the flow path. Therefore, it is essential to also study how the flow rate of gas and liquid affects the bubbles in the bubble layer prior to clogging, which will be discussed next.

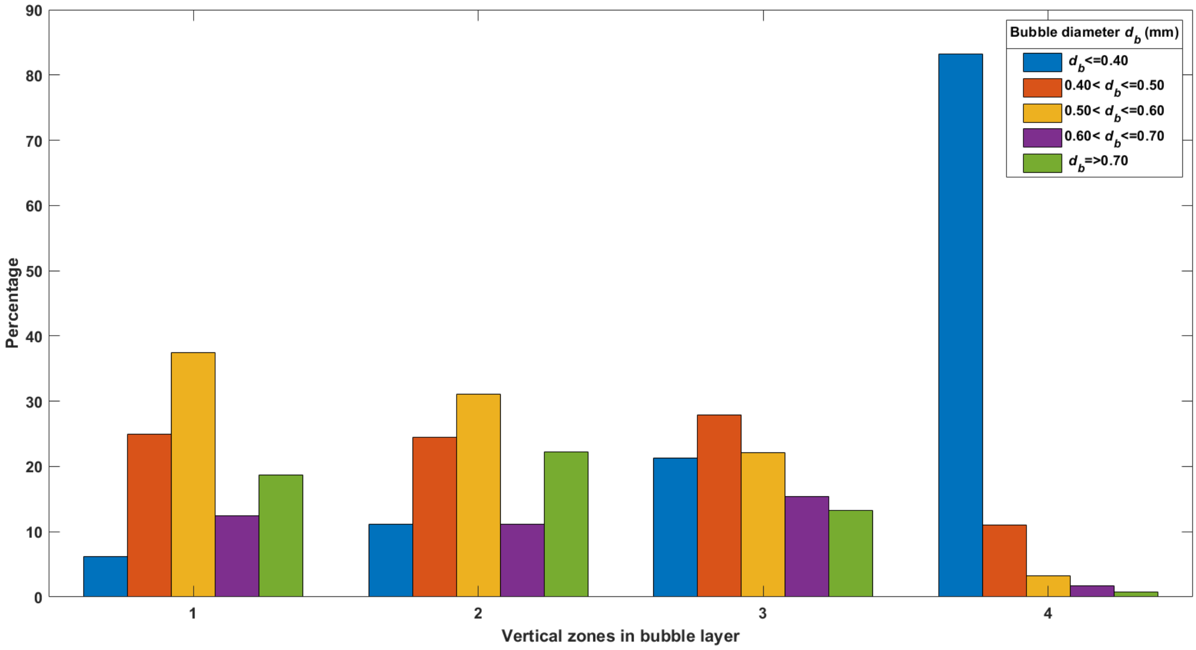

Figure 4.8: Bubble size distribution as a function of the bubble layer region. Region 1 represents the top zone of the bubble layer, while region 4 represents the bottom region. The smallest bubbles appear in the bottom region of the bubble layer.

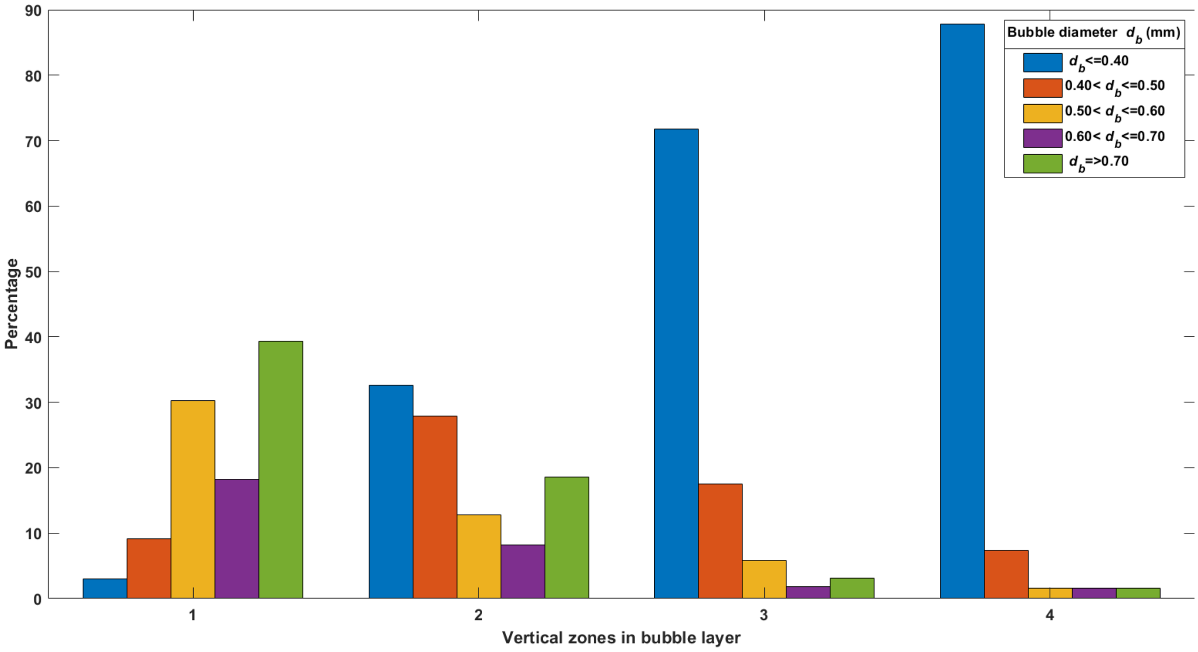

Figure 4.9: Bubble size distribution as a function of the bubble layer region. The zones are shown in the x-axis. The smallest bubbles appear in the bottom region of the bubble layer.

Bubble layer thickness and velocity

Now that the bubble diameters have been determined, we will analyze the dynamics of the bubble layer. From the experiments, it appeared that the risen bubbles move in a train at the slanted top of the chamber. This bubble layer has a certain thickness and moves at a uniform velocity along its length. The thickness and velocities of the bubble layer were investigated at different current densities and pump rates. The corresponding flow rates for the evaluated pump rates are provided in Table 4.4.

Table 4.4: Pump rates and associated flow rates through each chamber.

Pump rate (RPM)	Flow rate (mL/s)
50	1.26
100	3.57
200	6.25

Figure 10 to Figure 13 in Appendix D show bubble layers at different current densities and pump flow rates. For each high-speed video (HSV), six random frames were chosen and analyzed. The thickness of the bubble layer was measured at locations where it was thickest using ImageJ. The mean thickness and standard deviation of the layer were then calculated and plotted against the current density and pump rate, as illustrated in Figure 4.10.

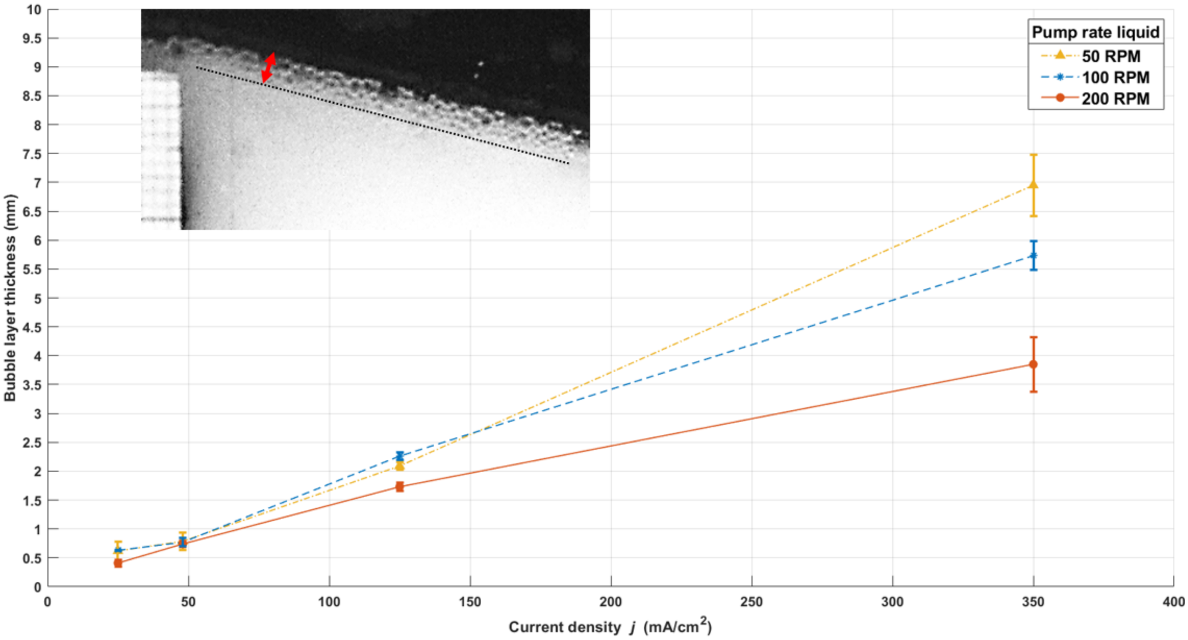

Figure 4.10: Bubbles layer thickness as a function of flow rate and current density. The layer thickness increases with increasing current density. At low current densities, the bubble layer thickness is less dependent on liquid flow rate. However, at larger current densities, it strongly depends on the liquid flow rate.

Given the figure above, it appears that at lower current densities (j < 50 mA/cm^2), there is no significant difference in bubble layer thickness with increasing flow rate. However, with high current densities (j > 300 mA/cm^2), there is a perceptible change in the thickness of the bubble layer, showing that the thickness decreases with increasing flow rate. For example, when the current density is 350 mA/cm^2, the mean thickness of the bubble layer at a flow rate of 3.57 mL/s is 18% smaller compared to the bubble layer at a flow rate of 1.26 mL/s. At a flow rate of 6.25 mL/s, the thickness is 33% smaller compared to the thickness of the bubble layer at a flow rate of 3.57 mL/s and 45% smaller compared to a flow rate of 1.26 mL/s. We can therefore surmise that the thickness of the bubble layer at the slanted top is substantially dependent on the liquid flow rate at higher current densities.

To investigate whether the same dependency holds for the bubble layer velocity, we tracked the bubbles at varying liquid flow rates and current densities. From each HSV, six arbitrary bubbles were tracked frame by frame at random locations in the bubble layer, and a mean velocity and standard deviation were calculated. The results of the bubble layer velocities are shown in Figure 4.11.

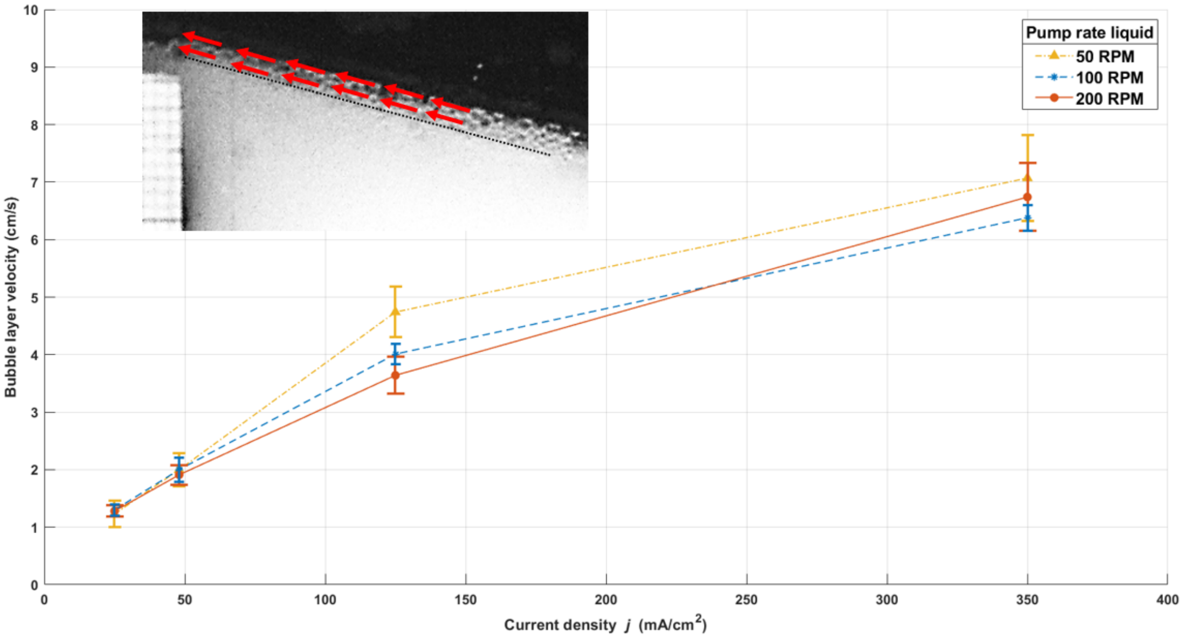

Figure 4.11: Bubble layer velocity for as a function of the flow rate and current density. The velocities are close to one another despite the difference in liquid flow rate.

The figure indicates that the bubble layer velocities are close to each other for most current densities, especially at lower ones. At a current density of j = 17.5 mA/cm^2 and at a pump rate of 200 RPM, the average velocity of the bubble layer is only 10% higher compared to the average velocity at the pump rate of 50 RPM. At higher current densities, such as j = 350 mA/cm^2, the average velocity at 200 RPM is approximately 30% higher than the average velocity at 50 RPM observed. However, because of irregularities of the flow, the standard deviation is higher at higher current densities. These inconsistencies were induced by the large number of bubbles generated, and therefore not all of the bubbles in the (thicker) bubble layer had uniform velocities. These findings suggest that the liquid flow rate has little effect on the velocity of the bubble layer, especially at low current density.

To determine whether there was a difference between the cathode flow and the anode flow that may have affected the velocity of the bubble layer, the temperature profile was also monitored throughout the experiments. The temperature data are presented in Figure 4.13a.

The graph reveals that the temperatures in the cathode and anode chambers are not significantly different during water electrolysis. They rise steadily with the same slope, indicating that the flow rate on both sides was roughly the same. However, it was observed that when the power was abruptly turned off at the end of an experiment, the channel immediately got blocked by accumulated bubbles, forcing the liquid to flow through the anode. This can be ascribed to the hydraulic configuration in which the liquid flow chooses to follow the path that presents the least resistance. This blockage did not occur when the power was dropped more gradually. Images of channel blockage after the power was abruptly turned off are depicted in Figure 4.12.

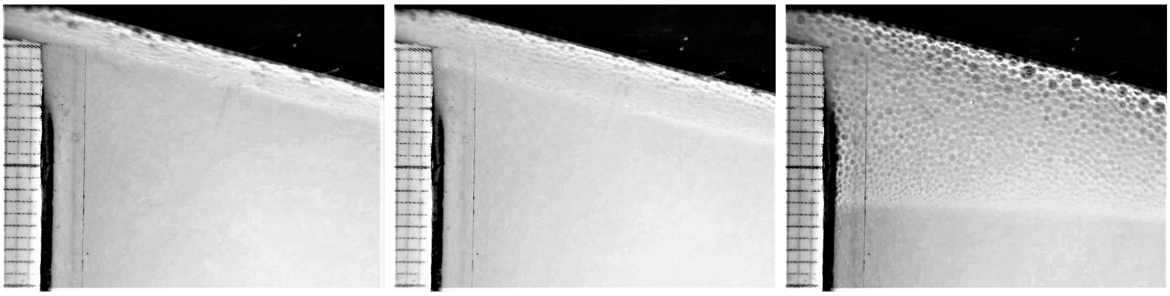

(a) t = 0 s **(b)** t = 1 s **(c)** t = 4 s

Figure 4.12: Bubbles on the cathode side restrict the outflow once the power is abruptly switched off at t = 0.

From the temperature profile shown in Figure 4.13b, the impact of channel blockage can be seen by the sharp drop in temperature on the anode side. This sharp drop is caused by the fresh electrolyte that flows through the anode side. Natural convection causes the temperature on the cathode side to decline more gradually.

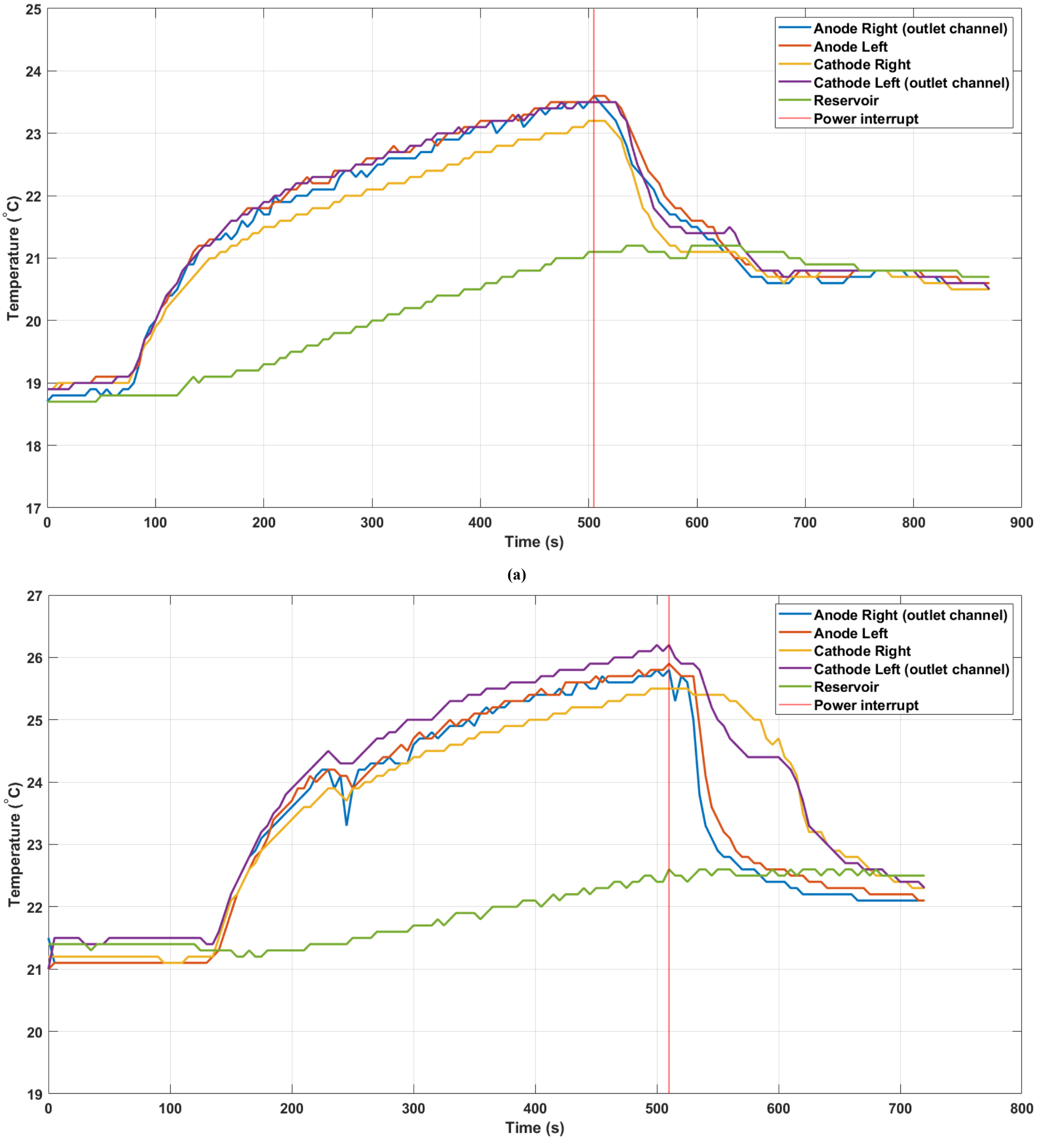

(a)

(b)

Figure 4.13: Temperature plot of the reservoir, the cathode chamber and anode chamber in a single cell electrolyzer stack. Each chamber had two thermocouples installed. The experiments were conducted at a current density of j = 350 mA/cm^2 and cell potential of U_{cell} = 2.60 V. (a) shows the temperature profile when the power was decreased gradually. (b) shows the temperature profile when the power was switched off instantaneously. Because of the necessity for ventilation, each experiment took around ten minutes.

Congestion flow regimes

The flow regimes in which clogging occurred were experimentally determined. The current and flow rate were the parameters that were varied during this experiment. The current density was converted to a (vertical) superficial gas velocity w_{SG} via Equation 2.16. The (vertical) superficial liquid velocity w_{SL} was determined using the high-speed camera. With the scale affixed to the plate, the rise in the liquid level was recorded and translated into an absolute liquid rise velocity, which was subsequently assumed as the superficial liquid velocity. The liquid flow rate was regulated so that the liquid flow velocity ranged from 0 to 0.25 cm/s. This was because no clogging was apparent above a liquid velocity of 0.25 cm/s. On the other hand, the current (and thus the superficial gas velocity) was raised until the blockages still persisted. Subsequently, the current was increased until no visible blockages were observed. This was until a superficial gas velocity of 0.3 cm/s.

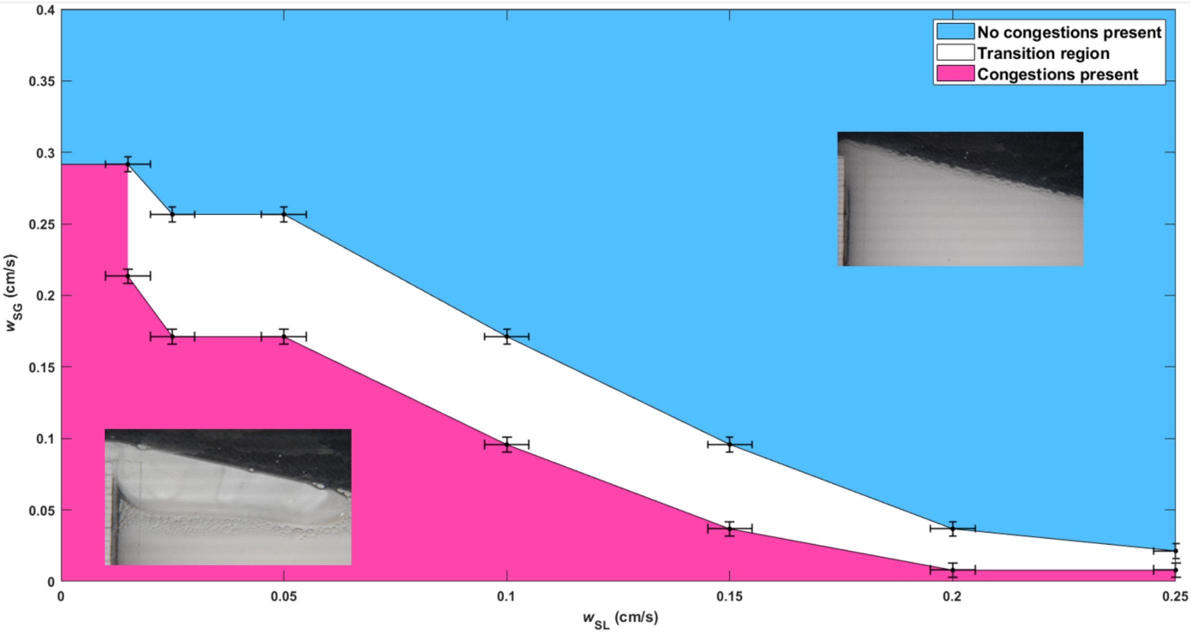

Figure 4.14: A plot of the flow regimes where blockages occur at the outlet channel. There is a transition region in which clogging tends to take place or still takes place but disappears periodically. The plot shows that above a certain superficial liquid velocity w_{SL} and gas velocity w_{SG}, there is a region in which no clogging occurs anymore.

Figure 4.14 shows the flow regimes in which clogging occurs. The graph reveals that there is a transition region where blockages persist but dissipate continuously. It also demonstrates the necessity of having a sufficiently high superficial liquid or gas velocity to prevent a clog from developing at the outlet channel. In other words, according to the graph, clogging can be avoided at large current densities or pumping power of the liquid. These observations are crucial because they teach future operators about flow regimes that are safe for operation.

It was also observed that once the clogging occurred, it vanished instantaneously once the superficial gas velocity was increased until the blue flow regime in Figure 4.14 (regime in which no congestion was present) entered. The superficial liquid velocity, however, required longer time to completely remove the slug when it was increased until the blue flow regime was reached.

A final observation was found when the experiments were performed without a pump. Without a pump and at a current density of approximately j = 140 mA/cm^2, there was still continuous bubble flow perceivable without clogging the channels. This can be attributed to the buoyancy forces of bubbles pushing other bubbles upward, resulting in a natural bubble flow that exits the chamber.

These results lead to the overall conclusion that there is no clogging at superficial gas flow rates greater than 0.3 cm/s and, consequently, current densities greater than 140 mA/cm ^{2}. When the liquid flow velocity surpasses 0.25 cm/s, the same appears to be the case.

5

Conclusions and recommendations

5.1. Conclusions

This thesis project aimed to experimentally investigate the minimum required flow conditions to prevent clogging in an alkaline water electrolyzer. The study involved conducting a literature research on fundamentals, bubble hydrodynamics, and leakage currents in water electrolyzers. A laboratory-scale alkaline water electrolyzer was designed and constructed to carry out the experimental study. The electrolyzer was used to examine the clogging of the outlet channels on the hydrogen side.

The results of the experimental study showed that there is a specific flow regime in which clogging does not appear in the outlet channel. At current densities greater than 140 mA/cm^2, which corresponds to a gas flow velocity of approximately 0.3 cm/s, the velocity of the bubble layer prevents accumulated bubbles from restricting the flow through the exit channel. Additionally, a liquid flow velocity greater than 0.3 cm/s also prevents channel clogging for the investigated electrolyzer design. However, at lower current densities and liquid flow velocities, the likelihood of clogging increases, and it is dependent on both parameters. Moreover, there is a transition regime in which clogging still occurs, but the overall contributions of hydraulic resistance, bubble flow, and forced liquid flow are balanced, which frequently ameliorates the channel.

The hydraulic configuration is the primary cause of clogging, where the flow can prefer to go through the anode rather than the cathode. The flow does not force the created slug on the cathode side forward, allowing it to remain in the chamber and continue to expand due to coalescence with bubbles coming from below. These findings are critical for electrolyzer operators since they reveal that specific flow regimes should be avoided to prevent clogging in an electrolyzer stack. Then, precautions could be taken to improve performance and, most importantly, to enhance safety.

The study evaluated the bubble diameter distribution to identify the diameters of hydrogen bubbles that contribute to clogging. The evaluation showed that the mean diameter of the hydrogen bubble was approximately 0.4 mm, which is five times smaller than the channel height through which the bubbles must flow. The largest bubble present in the bubble layer was approximately two to three times the height of the channel. The flow velocities of the gas and liquid significantly affect the frequency of bubbles appearing in the bubble layer.

On the basis of these experimental findings, the following conclusions are made concerning the bubble layer thickness/velocity with respect to the gas flow and liquid flow rate.

1. The liquid flow rate does not significantly influence the thickness of the bubble layer at current densities less than 50 mA/cm^2. This could be due to a stable and well-defined bubble layer, which could be caused by a uniform flow in the bubble layer. At current densities greater than 140 mA/cm^2, the bubble layer clearly decreases with increasing liquid flow rate. This might be attributed to the more unstable bubbles in the chamber at higher current densities. With a faster liquid flow, the unstable bubbles are likely to be moved away more quickly, which might explain the difference in bubble layer thickness.
2. The liquid flow rate does not significantly affect the velocity of the bubble layer at current densities less than 50 mA/cm2. This could again be related to the stable bubble layer, which is less susceptible to changes in the liquid flow rate. Additionally, the gas flow rate is dominant in the bubble layer region, meaning that changing the liquid flow rate has little effect on the bubble layer velocity. However, at higher current densities, there is no clear relationship between bubble layer velocity and liquid flow rate, which may be due to experimental limitations.

3. The thickness and velocity of the bubble layer depend strongly on the applied current density. This can be clarified by the fact that the superficial gas velocity is directly proportional to the applied current density. Moreover, more bubbles are produced with higher current densities, and as a result of the buoyant forces generated by these bubbles, the overall bubble speed increases too.

5.2. Recommendations

To gain a deeper understanding of the clogging process in water electrolyzer stacks, it is recommended to conduct additional experiments, particularly in larger stacks consisting of numerous cells. The same experiments could be performed with highspeed camera in combination with a microscope lens in order to examine the bubble interactions that lead to clogging more closely. In addition, more data points should be examined in the experiments for the bubble layer thickness/velocity.

However, visually monitoring all cells in an industrial-size electrolyzer stack can be challenging. To address this, low-cost temperature sensors could be installed in all cells to provide an indication of flow within each cell.

Another area that requires further exploration is the clogging behavior of different channel shapes, dimensions, wall distances, and angles at which bubble layers are guided towards exit channels. These parameters play a critical role in bubble flow and must be studied as well to improve mass transport in electrolyzers.

To reduce the ohmic resistance of the current electrode design, it is recommended to create an improved design that allows the electric current to reach the entire electrode surface, rather than through flaps sticking out from the sides. This change has the potential to significantly improve the electrolyzer efficiency.

In addition, it is suggested to consider electrolyzers that do not require forced flow, which demands a significant amount of power. The experiments conducted showed that even without a pump, flow was still achievable at certain current densities. A techno-economic analysis should be conducted to investigate whether it is feasible to run larger scale electrolyzers without a pump or with less pumping power and compare the savings gained to the compression cost that is required for usage.

Lastly, it is recommended to examine the effect of slug flow through the channel in relation to shunt currents. This could be done by experimentally measuring shunt currents using reference electrodes mounted on the manifolds of the designed electrolyzer. With the theory of shunt currents and scaling relations provided in chapter 2, the relationship could be examined and compared to models.

References

[1] Global Carbon Project. "Global Carbon Budget 2022". In: *Earth System Science Data* 14.11 (Nov. 11, 2022), pp. 4811–4900. DOI: `10.5194/essd-14-4811-2022`. URL: `https://essd.copernicus.org/articles/14/4811/2022/essd-14-4811-2022.pdf`.

[2] United Nations. "Paris agreement". In: (2015). URL: `https://unfccc.int/sites/default/files/english_paris_agreement.pdf` (visited on 10/04/2022).

[3] E. Hagedoorn. "Stoken op waterstof: deze 5 gemeenten doen het gewoon". In: (Oct. 17, 2018). URL: `https://stadszaken.nl/artikel/1864/stoken-op-waterstof-deze-5-gemeenten-doen-het-gewoon` (visited on 10/04/2022).

[4] D. Gosse. *Heating energy and process heat using climate-neutral hydrogen*. 2021. URL: `https://www.bosch-climate.cl/DescargarFiles/39466e21-5d8d-4f7c-b7b2-c08bf3d75812.pdf` (visited on 10/04/2022).

[5] G. Chisholm and L. Cronin. "Chapter 16 - Hydrogen From Water Electrolysis". In: *Storing Energy*. Ed. by Trevor M. Letcher. Oxford: Elsevier, 2016, pp. 315–343. ISBN: 978-0-12-803440-8. DOI: `https://doi.org/10.1016/B978-0-12-803440-8.00016-6`. URL: `https://www.sciencedirect.com/science/article/pii/B9780128034408000166`.

[6] *Electrolysis of Water - Solar Hydrogen Generation - Brian Williams*. Dec. 28, 2022. URL: `https://www.briangwilliams.us/solar-hydrogen-generation/electrolysis-of-water-1.html`.

[7] B. de Rooij, P.Widdows, and W. Nijhuis. "Innovative electrolyser for green hydrogen". Nederlands. In: ().

[8] Haverkort J.W. *Compact electrochemical stack using corrugated electrodes*. Nederlands. May 18, 2021. URL: `https://worldwide.espacenet.com/patent/search?q=pn%5C%3DNL2023775B1`.

[9] D. Santos, César Sequeira, and José Figueiredo. "Hydrogen production by alkaline water electrolysis". In: *Química Nova* 36 (Dec. 2012), pp. 1176–1193. DOI: `10.1590/S0100-40422013000800017`.

[10] M. Paidar J. Hnat and K. Bouzek. "5 - Hydrogen production by electrolysis". In: *Current Trends and Future Developments on (Bio-) Membranes*. Elsevier, 2020, pp. 91–117. ISBN: 978-0-12-817384-8. DOI: `https://doi.org/10.1016/B978-0-12-817384-8.00005-4`. URL: `https://www.sciencedirect.com/science/article/pii/B9780128173848000054`.

[11] H. Wendt and H Hofmann. "Ceramic diaphragms for advanced alkaline water electrolysis". In: *Journal of Applied Electrochemistry* 19 (Jan. 1989), pp. 1176–1193. DOI: `10.1007/BF01022121`.

[12] M. Schalenbach et al. "A Perspective on Low-Temperature Water Electrolysis – Challenges in Alkaline and Acidic Technology". In: *International Journal of ELECTROCHEMICAL SCIENCE* 13 (Dec. 2017), pp. 1173–1226. DOI: `110.20964/2018.02.26`.

[13] P. Gallone, L. Giuffré, and G. Modica. "Developments in separator technology for electrochemical reactors". In: *Electrochimica Acta* 28.10 (1983), pp. 1299–1307. ISSN: 0013-4686. DOI: `https://doi.org/10.1016/0013-4686(83)85181-0`. URL: `https://www.sciencedirect.com/science/article/pii/0013468683851810`.

[14] Matheus T. de Groot and Albertus W. Vreman. "Ohmic resistance in zero gap alkaline electrolysis with a Zirfon diaphragm". In: *Electrochimica Acta* 369 (2021), p. 137684. ISSN: 0013-4686. DOI: `https://doi.org/10.1016/j.electacta.2020.137684`. URL: `https://www.sciencedirect.com/science/article/pii/S0013468620320776`.

[15] MD Rashid et al. "Hydrogen production by water electrolysis: a review of alkaline water electrolysis, PEM water electrolysis and high temperature water electrolysis". In: *International Journal of Engineering and Advanced Technology* (2015).

[16] Robert Phillips and Charles Dunnill. "Zero Gap Alkaline Electrolysis Cell Designs for Renewable Energy Storage as Hydrogen Gas". In: *RSC Adv.* 6 (Oct. 2016), pp. 100643–100651. DOI: `10.1039/C6RA22242K`.

[17] A. Scharlau. “Wasserstoff-Erzeugung durch Druckelektrolyse von Wasser”. In: *Fette, Seifen, Anstrichmittel* 62.3 (), pp. 185–189. DOI: `https://doi.org/10.1002/lipi.19600620307`. eprint: `https://onlinelibrary.wiley.com/doi/pdf/10.1002/lipi.19600620307`. URL: `https://onlinelibrary.wiley.com/doi/abs/10.1002/lipi.19600620307`.

[18] N. Nagai et al. “Existence of optimum space between electrodes on hydrogen production by water electrolysis”. In: *International Journal of Hydrogen Energy* 28.1 (2003), pp. 35–41. ISSN: 0360-3199. DOI: `https://doi.org/10.1016/S0360-3199(02)00027-7`. URL: `https://www.sciencedirect.com/science/article/pii/S0360319902000277`.

[19] J.W. Haverkort and H. Rajaei. “Voltage losses in zero-gap alkaline water electrolysis”. In: *Journal of Power Sources* 497 (2021), p. 229864. ISSN: 0378-7753. DOI: `https://doi.org/10.1016/j.jpowsour.2021.229864`. URL: `https://www.sciencedirect.com/science/article/pii/S037877532100402X`.

[20] Maximilian Schalenbach et al. “A Perspective on Low-Temperature Water Electrolysis – Challenges in Alkaline and Acidic Technology”. In: *International Journal of Electrochemical Science* 13 (Feb. 2018), pp. 1173–1226. DOI: `10.20964/2018.02.26`.

[21] Kai Zeng and Dongke Zhang. “Recent progress in alkaline water electrolysis for hydrogen production and applications”. In: *Progress in Energy and Combustion Science* 36.3 (2010), pp. 307–326. ISSN: 0360-1285. DOI: `https://doi.org/10.1016/j.pecs.2009.11.002`. URL: `https://www.sciencedirect.com/science/article/pii/S0360128509000598`.

[22] R.L. LeRoy. “Industrial water electrolysis: Present and future”. In: *International Journal of Hydrogen Energy* 8.6 (1983), pp. 401–417. ISSN: 0360-3199. DOI: `https://doi.org/10.1016/0360-3199(83)90162-3`. URL: `https://www.sciencedirect.com/science/article/pii/0360319983901623`.

[23] A. T. Kuhn and J. S. Booth. “Electrical leakage currents in bipolar cell stacks”. In: *Journal of Applied Electrochemistry* 10.2 (Mar. 1980), pp. 233–237. DOI: `10.1007/bf00726091`. URL: `http://dx.doi.org/10.1007/bf00726091`.

[24] R.L. LeRoy and A.K. Stuart. “Advanced unipolar electrolysis”. In: *International Journal of Hydrogen Energy* 6.6 (1981), pp. 589–599. ISSN: 0360-3199. DOI: `https://doi.org/10.1016/0360-3199(81)90024-0`. URL: `https://www.sciencedirect.com/science/article/pii/0360319981900240`.

[25] P. Bolomey Ch. Comninellis E. Plattner. “Estimation of current bypass in a bipolar electrode stack from current-potential curves”. In: *Journal of Applied Electrochemistry* 21.5 (May 1991), pp. 415–418. DOI: `10.1007/bf01024577`. URL: `http://dx.doi.org/10.1007/bf01024577`.

[26] JC Burnett and DE Danly. “Current bypass in electrochemical cell assemblies”. In: 75 (1979), pp. 8–13.

[27] L.J.J. Janssen. “Mass transfer at gas evolving electrodes”. In: *Electrochimica Acta* 23.2 (1978), pp. 81–86. ISSN: 0013-4686. DOI: `https://doi.org/10.1016/0013-4686(78)80101-7`. URL: `https://www.sciencedirect.com/science/article/pii/0013468678801017`.

[28] P. Byrne. “An experimental investigation of bubble-induced free convection in a small electrochemical cell”. In: *Journal of Applied Electrochemistry* 30.7 (2000), pp. 767–775. DOI: `10.1023/a:1004034807331`. URL: `http://dx.doi.org/10.1023/a:1004034807331`.

[29] Fumio Hine and Koichi Murakami. “Bubble Effects on the Solution IR Drop in a Vertical Electrolyzer Under Free and Forced Convection”. In: *Journal of The Electrochemical Society* 127.2 (Feb. 1980), pp. 292–297. DOI: `10.1149/1.2129658`. URL: `https://doi.org/10.1149/1.2129658`.

[30] M.J. Prince and H.W. Blanch. “Bubble coalescence and break-up in air-sparged bubble columns”. In: *AIChE Journal* 36.10 (1990), pp. 1485–1499. DOI: `https://doi.org/10.1002/aic.690361004`. URL: `https://aiche.onlinelibrary.wiley.com/doi/abs/10.1002/aic.690361004`.

[31] F. Hine et al. “Hydrodynamic Studies on a Vertical Electrolyzer with Gas Evolution under Forced Circulation”. In: *Journal of The Electrochemical Society* 131.1 (Jan. 1984), pp. 83–89. DOI: `10.1149/1.2115551`. URL: `https://doi.org/10.1149/1.2115551`.

[32] R. J. Balzer and H. Vogt. “Effect of Electrolyte Flow on the Bubble Coverage of Vertical Gas-Evolving Electrodes”. In: *Journal of The Electrochemical Society* 150.1 (2003), E11. DOI: `10.1149/1.1524185`. URL: `https://doi.org/10.1149/1.1524185`.

[33] Soufiane Abdelghani-Idrissi et al. “Effect of electrolyte flow on a gas evolution electrode”. In: *Scientific Reports* 11.1 (Feb. 2021). DOI: `10.1038/s41598-021-84084-1`. URL: `https://doi.org/10.1038/s41598-021-84084-1`.

[34] Dongke Zhang and Kai Zeng. “Evaluating the Behavior of Electrolytic Gas Bubbles and Their Effect on the Cell Voltage in Alkaline Water Electrolysis”. In: *Industrial and Engineering Chemistry Research* 51.42 (2012), pp. 13825–13832. DOI: `10.1021/ie301029e`. eprint: `https://doi.org/10.1021/ie301029e`. URL: `https://doi.org/10.1021/ie301029e`.

[35] Hadi Rajaei, Aviral Rajora, and J.W. (Willem) Haverkort. “Design of membraneless gas-evolving flow-through porous electrodes”. In: *Journal of Power Sources* 491 (Apr. 2021), p. 229364. DOI: `10.1016/j.jpowsour.2020.229364`.

[36] C.W.M.P. Sillen et al. “Gas bubble behaviour during water electrolysis”. In: *International Journal of Hydrogen Energy* 7.7 (1982), pp. 577–587. ISSN: 0360-3199. DOI: `https://doi.org/10.1016/0360-3199(82)90038-6`. URL: `https://www.sciencedirect.com/science/article/pii/0360319982900386`.

[37] Herbert H. Kellogg. “Anode Effect in Aqueous Electrolysis”. In: *Journal of The Electrochemical Society* 97.4 (1950), p. 133. DOI: `10.1149/1.2777980`. URL: `https://doi.org/10.1149/1.2777980`.

[38] Hubert Chanson. “11 - Unsteady open channel flows: 1. Basic equations”. In: (2004). Ed. by Hubert Chanson, pp. 185–222. DOI: `https://doi.org/10.1016/B978-075066165-2.50044-8`. URL: `https://www.sciencedirect.com/science/article/pii/B9780750661652500448`.

[39] *Lognormal Distribution- MATLAB & Simulink- MathWorks Benelux*. URL: `https://nl.mathworks.com/help/stats/lognormal-distribution.html`.

[40] Julien Durst et al. “New insights into the electrochemical hydrogen oxidation and evolution reaction mechanism”. In: *Energy and Environmental Science* 7 (Apr. 2014), p. 2255. DOI: `10.1039/C4EE00440J`.

[41] Foteini M. Sapountzi et al. “Electrocatalysts for the generation of hydrogen, oxygen and synthesis gas”. In: *Progress in Energy and Combustion Science* 58 (2017), pp. 1–35. ISSN: 0360-1285. DOI: `https://doi.org/10.1016/j.pecs.2016.09.001`. URL: `https://www.sciencedirect.com/science/article/pii/S0360128516300260`.

[42] Tatsuya Shinagawa, Angel Garcia-Esparza, and Kazuhiro Takanabe. “Insight on Tafel slopes from a microkinetic analysis of aqueous electrocatalysis for energy conversion”. In: *Scientific reports* 5 (Sept. 2015), p. 13801. DOI: `10.1038/srep13801`.

[43] Meng Ni, Michael K.H. Leung, and Dennis Leung. “Electrochemical modeling of hydrogen production by proton-conducting solid oxide steam electrolyzer”. In: *International Journal of Hydrogen Energy - INT J HYDROGEN ENERG* 33 (Aug. 2008), pp. 4040–4047. DOI: `10.1016/j.ijhydene.2008.05.065`.

[44] Renato Seeber, Chiara Zanardi, and Gyorgy Inzelt. “Links between electrochemical thermodynamics and kinetics”. In: *ChemTexts* 1 (Sept. 2015). DOI: `10.1007/s40828-015-0018-9`.

[45] Jesús Rodríguez et al. “Simple and Precise Approach for Determination of Ohmic Contribution of Diaphragms in Alkaline Water Electrolysis”. In: *Membranes* 9.10 (2019). DOI: `10.3390/membranes9100129`. URL: `https://www.mdpi.com/2077-0375/9/10/129`.

Appendix A

Overpotentials

Activation overpotential

The activation overpotential η_{act} represents the overpotential that is required to overcome the activation barrier of a chemical reaction. It is also a measure of the activity of the electrodes. In order to have a better grasp of the mechanics underlying these barriers, this subject will be discussed in more detail. As indicated in Equation 2.5, the activation part is composed of two terms; the anodic term and the cathodic term, respectively. These activation terms are linked to the two half-reactions in AWE.

Hydrogen evolution reaction (HER) occurs on the cathodic side of the electrodes. This reaction consists of three steps, and when added together, they yield the cathodic half reaction shown in Equation 1.1. It is a well-understood process, as evidenced by various scientific studies in the literature [40, 41, 42]. The first step of the HER, also known as the Volmer step [10], involves a water molecule that, in the presence of an electron, splits into an adsorbed hydrogen atom on the surface and a hydroxide ion. This Volmer step is given in Equation 1.

$$\mathrm{H_2O} + \mathrm{e}^- = \mathrm{H_{ads}} + \mathrm{OH}^- \qquad \text{(Volmer)} \tag{1}$$

For the next step, the adsorbed hydrogen atom has two options. In one route, it can react with water to form a hydrogen molecule and hydroxide ion, as given in Equation 2 (also known as the Heyrovsky step). Alternatively, it can recombine with another $\mathrm{H_{ads}}$ to only yield $\mathrm{H_2}$, which is also known as the Tafel step, shown in Equation 3. Overall, there are two reactions occurring in series, with only one intermediate. Therefore, overcoming this barrier is, in general, not too difficult.

$$\mathrm{H_2O} + \mathrm{H_{ads}} + \mathrm{e}^- = \mathrm{H_2} + \mathrm{OH}^- \qquad \text{(Heyrovsky)} \tag{2}$$

$$\mathrm{H_{ads}} + \mathrm{H_{ads}} = \mathrm{H_2} \qquad \text{(Tafel)} \tag{3}$$

In contrast, the Oxygen Evolution Reaction (OER) takes place on the anodic side, which is more complex compared to the HER. Despite the fact that there is controversy about the distinctive OER mechanisms, it is generally acknowledged that the oxygen evolution chain consists of four unique electron transferring steps [9, 21]. The OER-steps in an alkaline environment are shown in Equation 4 - 7. Since there are four reactions occurring and each one forms a barrier, it is more challenging to proceed with the OER. Therefore, a greater overpotential on the OER-side is necessary to stimulate the entire reaction.

$$\mathrm{OH}^- + \text{surface} = \mathrm{OH_{ads}} + \mathrm{e}^- \tag{4}$$

$$\mathrm{OH}^- + \mathrm{OH_{ads}} = \mathrm{O_{ads}} + \mathrm{H_2O} + \mathrm{e}^- \tag{5}$$

$$\mathrm{O_{ads}} + \mathrm{OH}^- = \mathrm{OOH_{ads}} + \mathrm{e}^- \tag{6}$$

$$\mathrm{OOH_{ads}} + \mathrm{OH}^- = \mathrm{O_2} + \mathrm{H_2O} + \mathrm{e}^- \tag{7}$$

The activation overpotential for a single step can be calculated using the Butler-Volmer equation given in Equation 8 [9]. The Butler-Volmer equation relates the net current density j to the applied (kinetic) overpotential η_{act}:

$$j = j_0 \left[\exp\left(\frac{\alpha F \eta_{\mathrm{act,i}}}{RT}\right) - \exp\left(\frac{(1-\alpha) F \eta_{\mathrm{act,i}}}{RT}\right) \right], \ \mathrm{i = a, c} \tag{8}$$

where j_0 is the exchange current density and α is the charge transfer coefficient. The exchange current density is a measure of how ready the electrodes are to carry out the electrochemical reaction. It can also be thought of as the activity of electron transfer under equilibrium conditions (i.e., when there is no overpotential applied), which provides information on the electrode's electrocatalytic performance. The higher the exchange current density, the higher the activity on the electrode surface [43]. The transfer coefficient α is a dimensionless number that, in physical terms, represents the fraction of the energy that goes towards the reduction/oxidation. For water electrolysis, the transfer coefficient is typically 0.5 [43].

By simplifying the Butler-Volmer equation, Equation 8 can be written as a function of η to finally yield the Tafel equation:

$$\eta = a + b\log(j) \tag{9}$$

where $a = \frac{2.303RT}{\alpha F}\log(j_0)$ and $b = \frac{2.303RT}{\alpha F}$. The Tafel slope, which is coefficient b in Equation 9 can be determined experimentally. The Tafel intercept a can be found by linearly extrapolating the curve from the Tafel (j vs. η) plot, as illustrated in Figure 1. With these values, the kinetic performance of various electrodes can be evaluated.

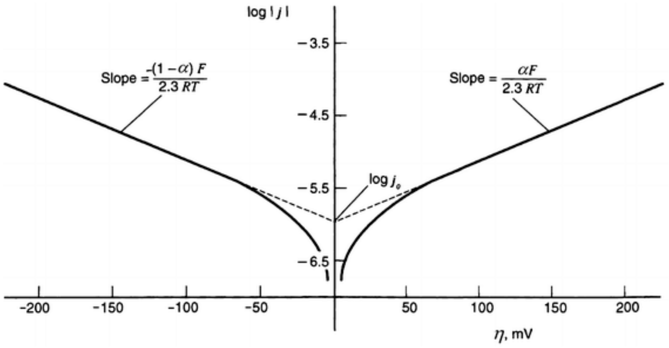

Figure 1: Tafel plot for anodic and cathodic portions of the j versus η curve. α = 0.5, T = 298 K, $j_0 = 10^{-6}$ A cm^{-2} [44]

Ohmic overpotential

The overpotential due to ohmic losses consists of four components: (i) resistance due to electric components; (ii) electrolytic resistance; (iii) resistance due to gas bubble formation; (iv) resistance caused by the membrane/diaphragm. The contributions of the ohmic components are illustrated in Figure 2.

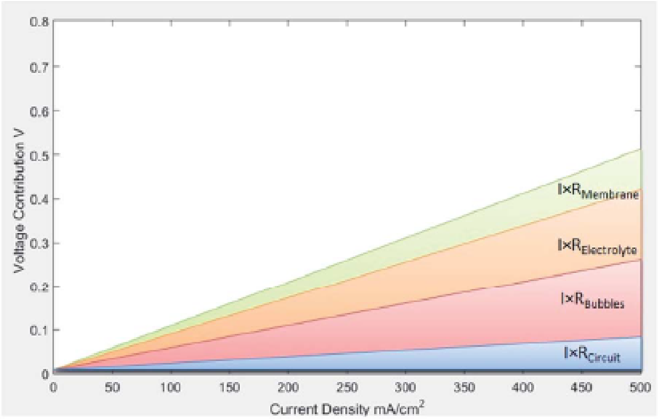

Figure 2: Components of the ohmic contributions [16]

(i) The resistance of the electric circuit can be determined with the type of material, the dimensions, and the conductivity of each individual component (e.g., electrodes, wires, connectors). The resistance R of a sample, such as a wire, can be calculated with the resistivity equation, which is simply a modified version of Equation 2.1:

$$R = \rho\frac{l}{A} \tag{10}$$

where ρ is the material-specific resistivity, l is the length of the specimen, and A is the cross-sectional area of the specimen. Note that in Equation 10, ρ is equal to $\frac{1}{\kappa}$. The ohmic resistance, for instance, can be decreased by shortening the wire lengths, expanding the cross section, or by selecting a material with a lower resistivity.

(ii) Electrolytic resistance has been briefly discussed in subsection 2.1.2. In fact, electrolytic resistance is also an example of electrical resistance, similar to electrical components. However, because the electrolyte is associated with a fluid and, therefore, its resistance dependence differs from that of a solid, it is discussed separately. For instance, electrolyte conductivity is also a function of the gas void fraction, which is the ratio of the volume that gas occupies in a channel to the total volume of the channel. Higher temperature also plays a role in the electrolyte conductivity, as it increases the activity of the medium.

(iii) Hydrogen/oxygen gas bubbles will inevitably form at the electrolyte-electrode interface as water electrolysis advances. Only when a bubble has grown sufficiently, it can detach from the electrode surface [21, 9]. A swarm of bubbles prevents the electrolyte from making contact with the electrode surface, hindering the electron transfer. Consequently, the resistance equation gains an additional ohmic drop term. Furthermore, the presence of bubbles in the electrolyte affects the electrolytic conductivity because bubbles reduce the active cross section in the electrolyte, resulting in higher resistances.

(iv) As mentioned previously, the diaphragm prevents the products at the anode and cathode from mixing to maintain chemical stability and safety. As a consequence, the diaphragm forms a barrier through which ions travel. The resistance of a diaphragm follows the same formula for the electrolyte, as shown in Equation 2.1, with the exception that the conductivity of a diaphragm is defined differently. The conductivity of a porous diaphragm can be determined with the following equation [45]:

$$\kappa_{\text{diaphragm}} = \frac{\kappa_{\text{el}}\,\epsilon}{\tau} \tag{11}$$

Where κ_{el} is the conductivity of the electrolyte that flows through the diaphragm and ϵ and τ are, respectively, the porosity and tortuosity of the diaphragm. The tortuosity is defined as the ratio of the effective path length (averaged) l_{eff} to the shortest path (thickness) $T_{diaphragm}$ in a diaphragm, given in Equation 12. The effective path length can be thought of as the shortest pathway in a diaphragm with added slack due to pores.

$$\tau = \frac{l_{\text{eff}}}{T_{\text{diaphragm}}} \tag{12}$$

Appendix B

Since the ionic shunt current can flow through the top and bottom manifold, this ionic pathway consists of a parallel circuit with two inlet and two outlet channels and two manifolds. When the manifold resistances are neglected, the total channel resistance R_{ch} becomes:

$$\frac{1}{R_{\text{ch}}} = \frac{2l_{\text{ch}}}{\kappa A_{\text{ch}}} + \frac{2l_{\text{ch}}}{\kappa A_{\text{ch}}} \tag{13}$$

For a stack of n cells and a voltage U for each cell, the current I from cell k to cell j becomes:

$$I_{kj} = \frac{U_{\text{cell}}}{R_{\text{ch}}}(j-k) \tag{14}$$

As a result, the net current inflow/outflow I_j can be expressed as:

$$I_j = \frac{U_{\text{cell}}}{R_{\text{ch}}}\sum_{k=1}^{n}(j-k) = \frac{U_{\text{cell}}}{R_{\text{ch}}}n\left(j - \frac{n+1}{2}\right) \tag{15}$$

From this expression, it can be found that the net current for the first half of the cells will be negative because it will be flowing out of the cells. For the second half, the sign will turn positive as there will be a net current flowing in the cells. For the center cell, no net current will flow in or out. The amount of bypassed current I_{bypass} between cell k and $k+1$ can be calculated with:

$$I_{\text{bypass}} = -\sum_{j=1}^{k}(I_j) = \frac{U_{\text{cell}}}{R_{\text{ch}}}\frac{kn}{2}(n-k) \tag{16}$$

This equation gives a parabolic shunt current profile, with a minimum at the edges and a maximum at the center of a stack.

According to Refs. [23], when analyzing the distribution of the (absolute) shunt current in a stack, the total shunt current in the header has a quadratic shape; it is the smallest at the ends and the largest in the middle of the stack, as illustrated in Figure 3a. This happens because when all individual shunt currents in the manifold are summed, the total shunt current flowing through the center of the manifold is at its maximum. Refs. [23] also states that ionic shunt current, flowing through the cell input and outlet channels, is S-shaped when plotted against the cell number. In other words, the shunt current is largest in magnitude in the outer cells where the largest potential difference exists, and smallest in the central cell, as shown schematically in Figure 3b. The sign of shunt currents in one half of the stack is opposite to the other half of the stack, which explains the S curve. The sign change is related to the net amount of current that flows into and out of a cell.

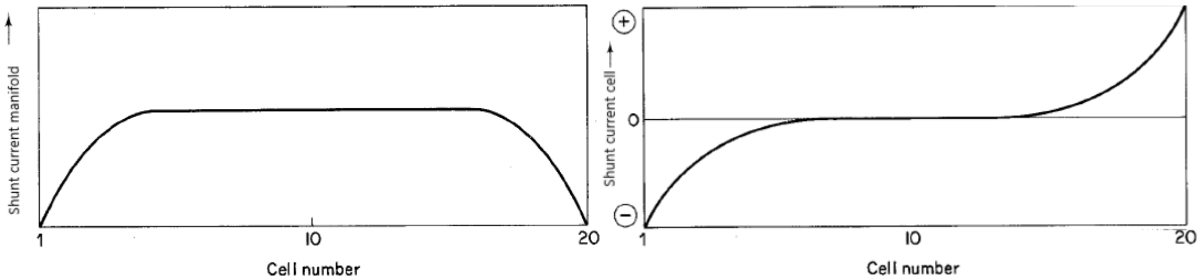

(a)

(b)

Figure 3: Schematic representation of the shunt currents flowing through the manifolds (a) and the inlet/outlet channels (b) in an electrolyzer stack consisting of N cells [23].

Graphical representations of Equation 13 for a stack with five cells are illustrated in Figure 4 and 5. For the sake of simplicity, shunt current flow in only one header is considered. The shunt current flow in the bottom manifold can be represented in a similar way. As an example, it is assumed that the voltage per cell is 2 V, which brings the total potential difference between the first and last cell to 10 V. For simplicity, the channel resistance of a single cell is taken to be 1Ω. The shunt current I_0 between two adjacent cells is then $I_0 = \frac{2V}{1\Omega} = 2A$. The shunt current flows in the same direction as the electrolyte, which is indicated with black arrows in all figures.

Furthermore, in Figure 6a, the net shunt current flow per cell is indicated with arrows. As shown, the first two cells have a negative sign, the cell in the middle has no net current flow, and the last two cells have a positive sign. Also, the total shunt current flow in the upper manifold is given in Figure 6a. A maximum current occurs in the middle of the cell.

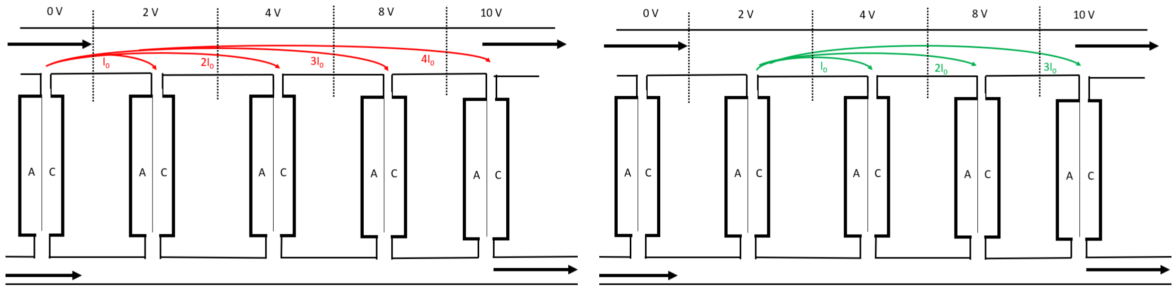

(a) **(b)**

Figure 4: Shunt outflow for cell 1 (a) and 2 (b)

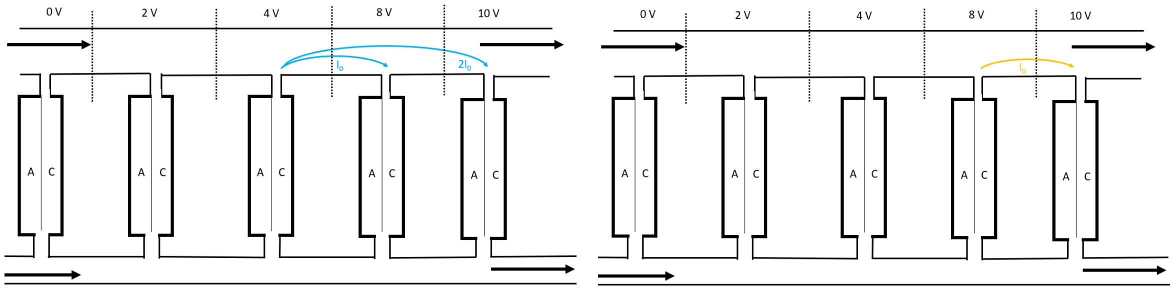

(a) **(b)**

Figure 5: Shunt outflow for cell 3 (a) and 4 (b)

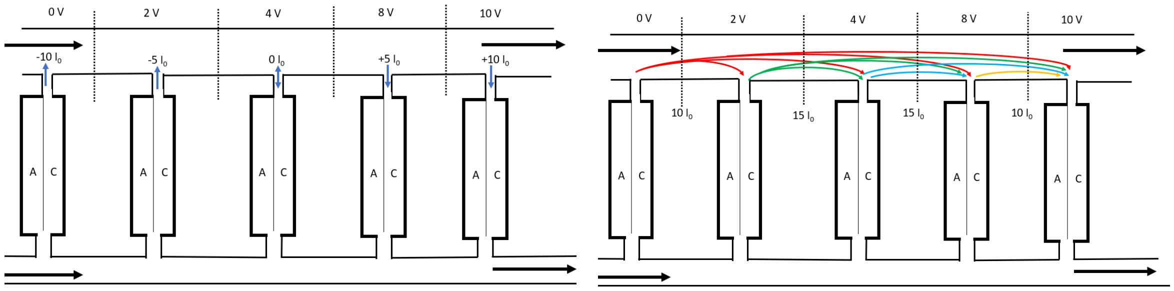

(a) **(b)**

Figure 6: Net shunt flow per cell (a) and total shunt current flow in the manifold, indicated with dotted lines (b)

Appendix C

In this appendix, the prototype of the BEP group will be analyzed. The prototype stack has a rectangular shape and is 80mm wide and 120mm tall. It consists of five cells, each 9mm thick and pressed to each other. The electrolyte enters the stack via a single bottom intake channel that is directly connected to the inlet manifold. Similarly, the generated hydrogen and oxygen can escape the stack individually through two top exit channels, connected to exit manifolds. The electrolyzer and an exploded view of the internal parts are shown in Figure 7 and 8 respectively. The following parts were used for the assembly:

- PMMA plates; used for the structural integrity of a cell. In addition, the plates have channels inside that act as inlets for the electrolyte and exits for the products. Manifolds are also integrated into plates.
- Zirfon Perl UTP 500 diaphragms; used to separate the chambers containing hydrogen or oxygen products.
- Corrugated stainless steel electrodes (anode and cathode) for electrolysis. An electrode has a total surface area of 12.23 cm^2 at each face.
- EPDM gaskets; used to seal the space between cells and the PMMA surface. They are also used to prevent electrodes from contacting each other and causing a short circuit.
- ABS clamping blocks, which have two functions. The first is to give the diaphragm a corrugated shape and match the shape of the stainless steel electrodes. The second function is to distribute the incoming electrolyte from the inlet channels and to direct the products toward the exit channel.
- Threads, nuts, and washers; for tightening the cells.
- Hose connectors; to attach inlet and outlet hoses
- Electric wires; to connect anodes to cathodes, and thus forming a bipolar 'plate'.

Three points should be noted in relation to the prototype. Firstly, the anodic and cathodic electrodes are perforated and have corrugated shapes. While the corrugated design increases the reaction surface area per volume of a unit cell, the perforations ensure that bubbles can escape more easily. The second remark is related to the configuration of how the electrodes are interconnected. In subsection 2.1.5, the bipolar arrangement was discussed and in Figure 2.4b, a bipolar plate was shown as a single plate with two polarities. Furthermore, it was mentioned that the order of polarity could be expressed as 'ACACACAC...' due to the alternating polarities. However, the design of the student group features an 'ACCAACCAAC...' sequence of polarities that is obtained by switching the electrodes from position after each cell. Each electrode pair is externally linked with electric wires, enabling the electrode pair to perform as a bipolar plate. An illustration of how the electrodes are connected is shown in Figure 9a. One significant benefit of such a structure is that the products are less exposed to each other as a result

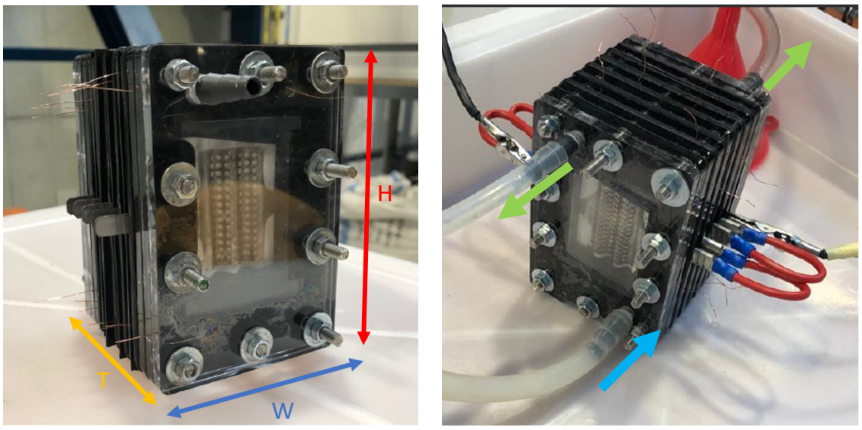

(a) **(b)**

Figure 7: The prototype version of recent BEP students [7]. (a) Height H is 120 mm, width W is 80 mm and thickness T is 60 mm. (b) Blue arrow at bottom indicates electrolyte inlet, green arrows at the top indicate the outlet of the product (O_2 or H_2)

of the reduced number of alternations between the oxidation and reduction chambers of the cells. This is crucial because a hydrogen-oxygen mixture poses a risk of explosion, and thus the concerned configuration enhances the operational safety. The final remark is about the packaging of the cells; the electrodes are pressed to each other with a diaphragm in between. This compact form of packaging is known as the zero-gap configuration and was already discussed in subsection 2.1.2.

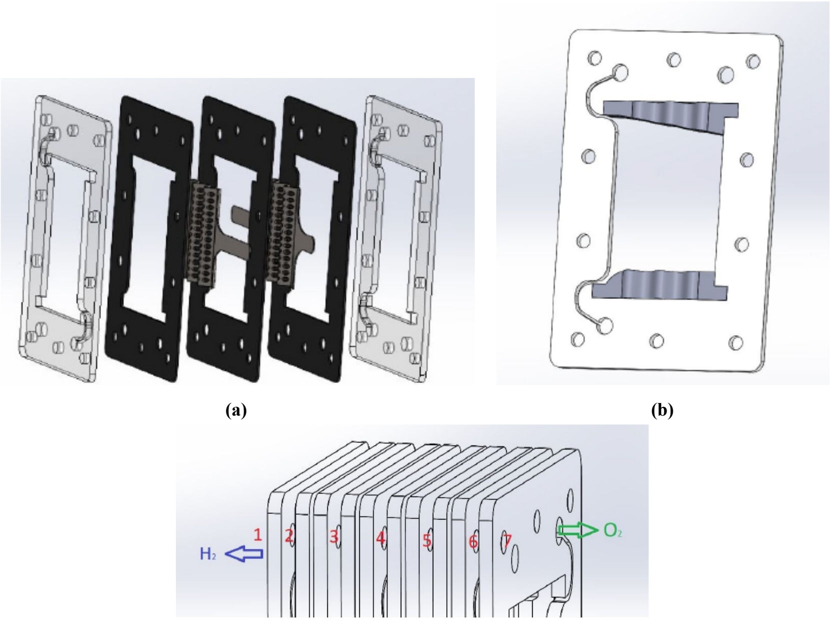

(a)

(b)

(c)

Figure 8: Exploded view showing the order of PMMA plates, gaskets, and electrodes in (a), a frontal view of a PMMA plate with clamping blocks in (b), and the flow direction of the products in (c) [7]

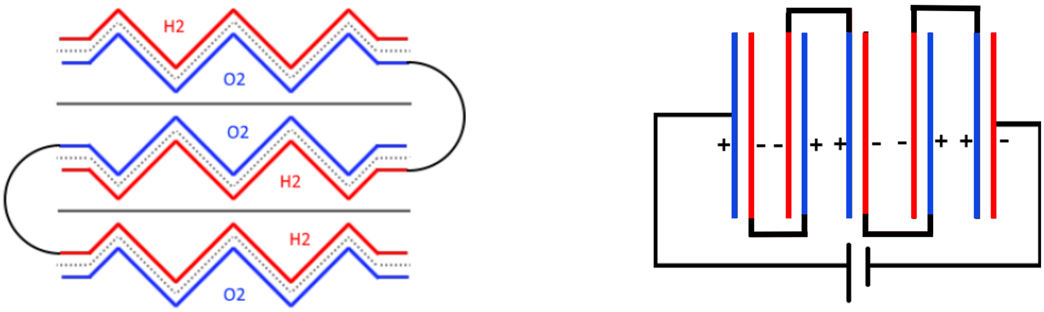

(a)

(b)

Figure 9: The bipolar configuration applied in the prototype [7]. (a) Shows the products produced at the electrodes and (b) shows the polarization of the electrodes.

Appendix D

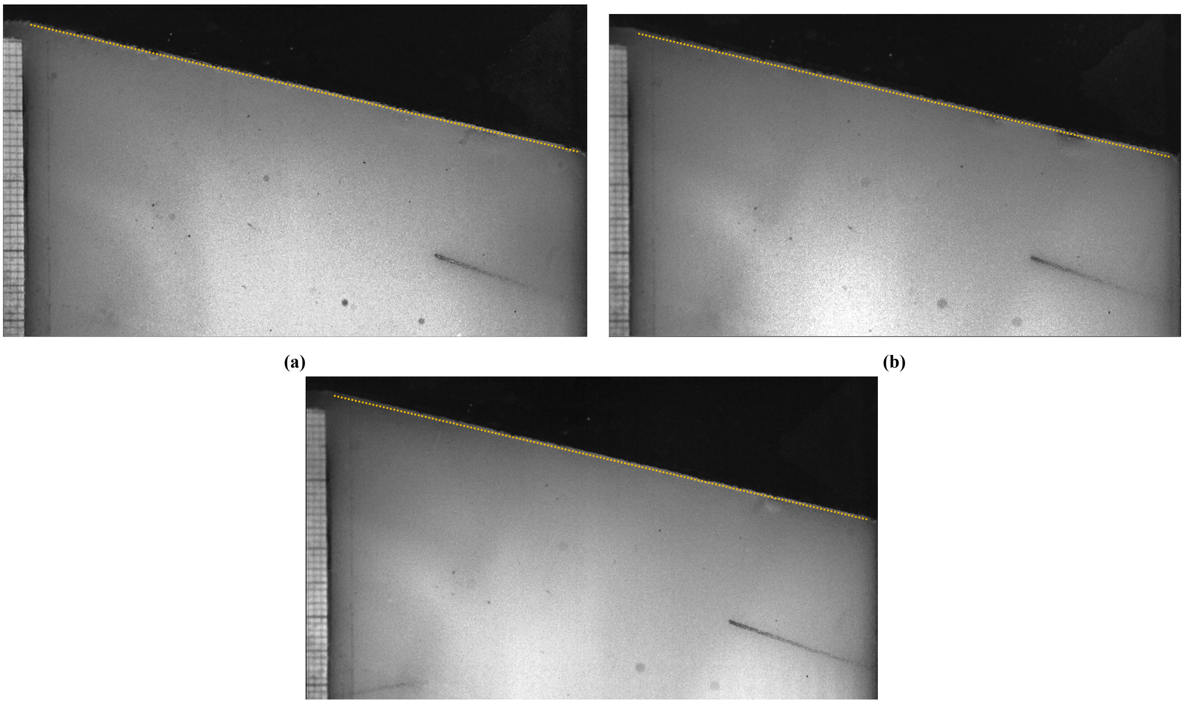

(a)

(b)

(c)

Figure 10: The bubble layer thickness at *j* = 25 mA/cm^2 for (a) 50 rpm, (b) 100 rpm and (C) 200 rpm

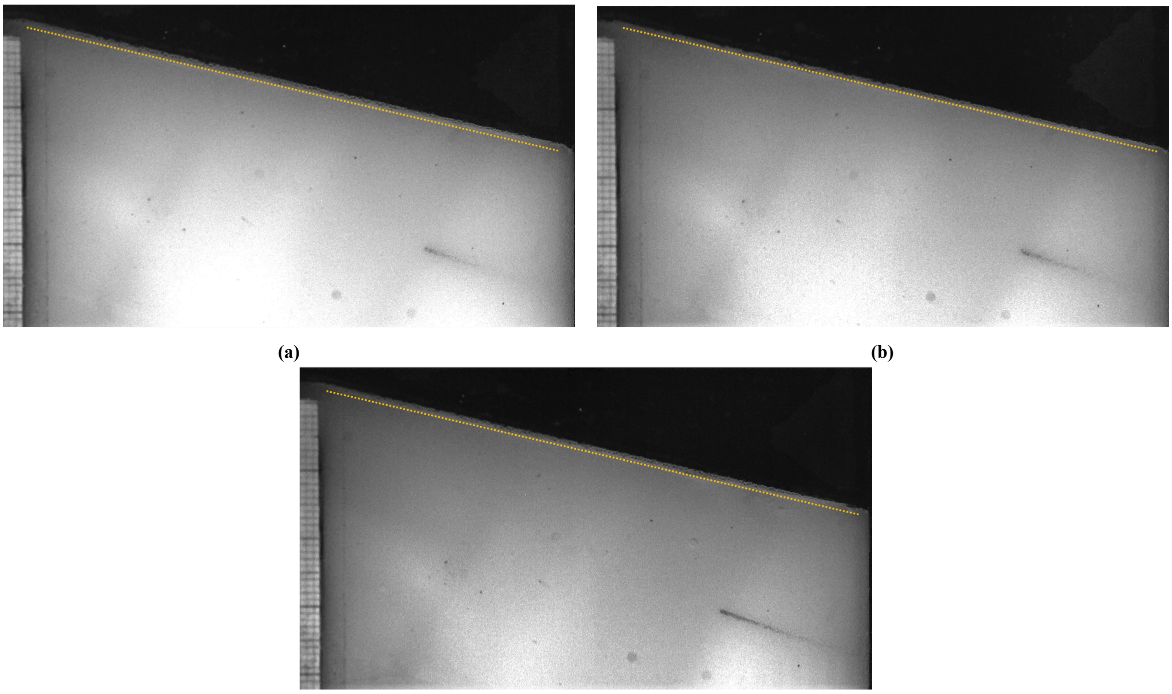

(a)

(b)

(c)

Figure 11: The bubble layer thickness at *j* = 48 mA/cm^2 for (a) 50 rpm, (b) 100 rpm and (C) 200 rpm

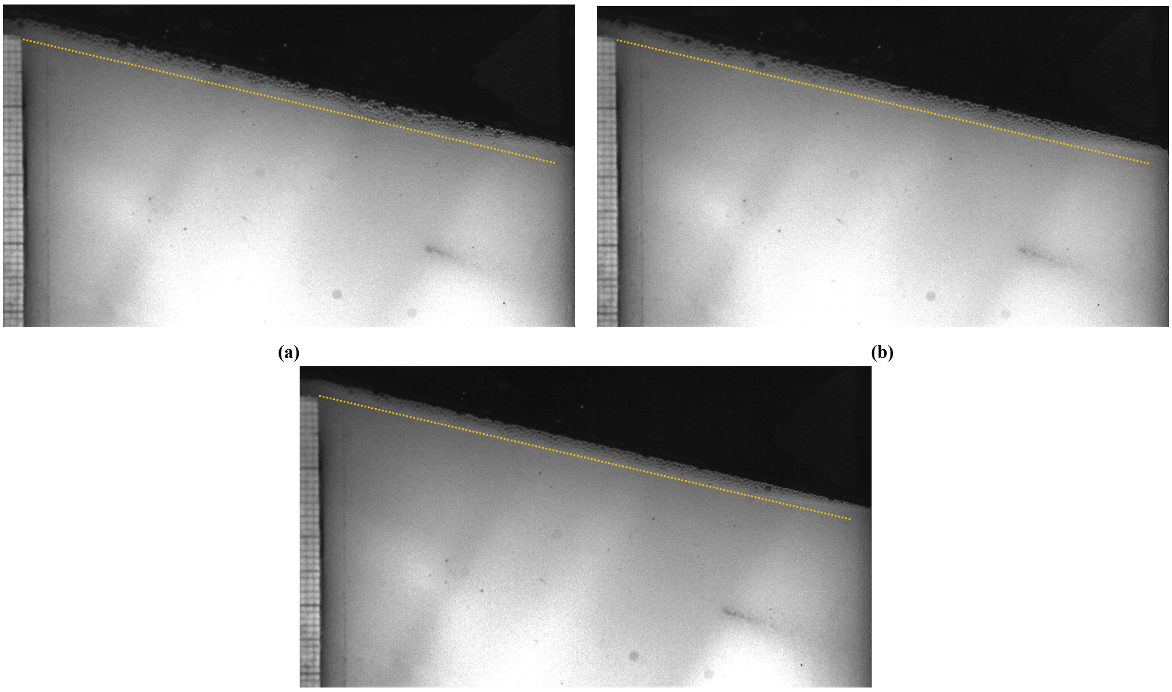

(a)

(b)

(c)

Figure 12: The bubble layer thickness at *j* = 125 mA/cm^2 for (a) 50 rpm, (b) 100 rpm and (C) 200 rpm

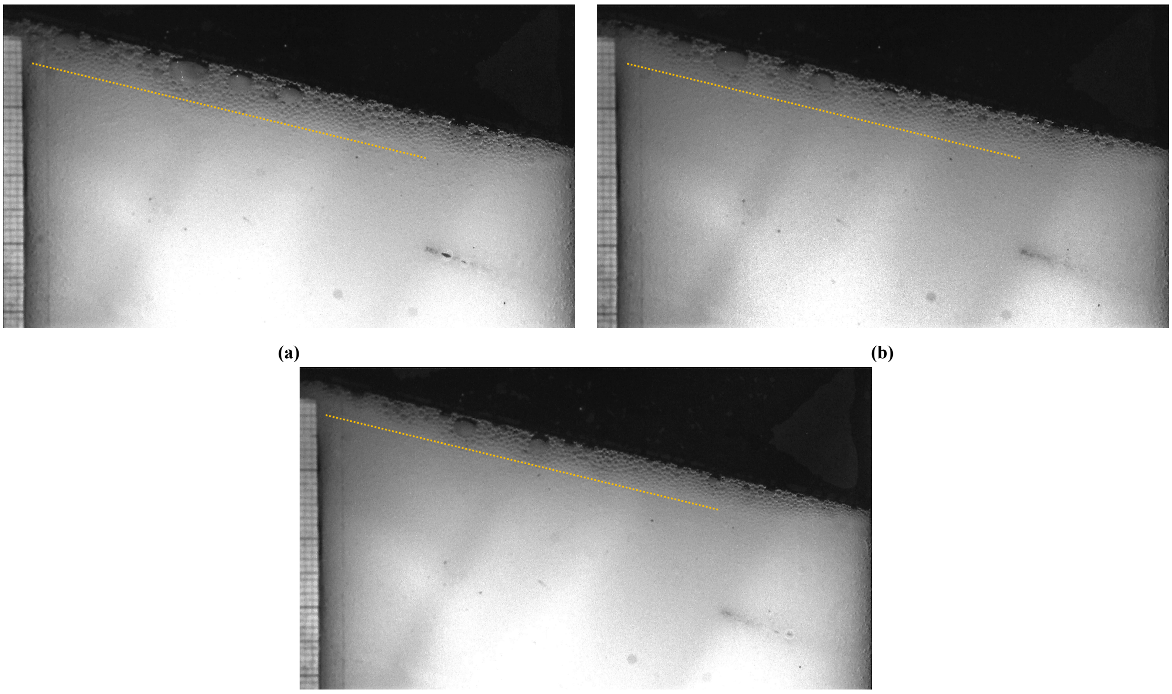

(a) **(b)**

(c)

Figure 13: The bubble layer thickness at *j* = 350 mA/cm^2 for (a) 50 rpm, (b) 100 rpm and (C) 200 rpm